metals

MDPI

Article

Effect of Hot Isostatic Pressing Temperature on Microstructure and Properties of TC21 Titanium Alloy

Haiyang Zhang [1], Chenyang Li [2], Jun Yin [2], Zhuan Qi [2], Ke Hua [1,*], Haifeng Wang [1] and Weimin Liu [1]

[1] State Key Laboratory of Solidification Processing, Center of Advanced Lubrication and Seal Materials, Northwestern Polytechnical University, Xi'an 710072, China
[2] Yinchuang Aerospace Industry (Jiangsu) Co., Ltd., Wu'xi 214000, China
* Correspondence: ke.hua@nwpu.edu.cn

Abstract

Powder metallurgy combined with hot isostatic pressing (PM-HIP) enables the fabrication of near-net-shape titanium alloy components with near-theoretical density, yet the HIP temperature fundamentally determines the densification behavior, phase constitution and mechanical properties of the consolidated alloy. In this work, TC21 pre-alloyed powder is consolidated by HIP at 890 °C, 920 °C, 950 °C, 980 °C and 1010 °C under 140 MPa for 3 h, followed by furnace cooling, and all the as-HIPed compacts are subsequently subjected to a two-step heat treatment (900 °C/1 h/air cooling + 590 °C/4 h/air cooling). The microstructure in both the as-HIPed and heat-treated states is characterized by SEM (scanning electron microscope), XRD (X-ray Diffraction), EBSD (Electron Back Scatter Diffraction) and TEM (transmission electron microscope), and the room-temperature tensile properties are evaluated. The results show that increasing the HIP temperature coarsens the primary α (α_p) and secondary α (α_s) phases while promoting the precipitation of α_s in the β matrix. The competition between the precipitation strengthening of α_s and microstructural coarsening governs the strength–ductility balance, and the alloy HIPed at 950 °C attains the optimum properties after heat treatment, with an ultimate tensile strength of 1259.5 ± 3.63 MPa, a yield strength of 1195.5 ± 3.5 MPa, an elongation to fracture of 13 ± 2.82% and a reduction of area of 35.5 ± 2.12%. The superior performance is attributed to the high volume fraction of fine α_s lamellae, which provides pronounced precipitation strengthening, together with an appropriate amount of α_p phase, which preserves strain-hardening capacity and ductility. These results clarify the HIP-temperature-dependent microstructure–property relationship of PM-HIP TC21 alloy and provide guidance for optimizing HIP parameters of powder-metallurgy titanium alloys.

Keywords: TC21; hot isostatic pressing temperature; heat treatment; mechanical properties

Academic Editor: Wislei Riuper Osório

Received: 25 August 2026
Revised: 30 September 2026
Accepted: 30 September 2026
Published: 7 October 2026

Copyright: © 2026 by the authors. Licensee MDPI, Basel, Switzerland. This article is an open access article distributed under the terms and conditions of the Creative Commons Attribution (CC BY) license.

1. Introduction

TC21 titanium alloy, with a nominal composition of Ti–6Al–2Sn–2Zr–3Mo–1Cr–2Nb–0.1Si (wt.%), is a high-strength damage-tolerant $\alpha + \beta$ titanium alloy that combines high specific strength, good corrosion resistance and low density, and has therefore been widely used in aerospace, biomedical and other fields [1–4]. It is typically employed for critical load-bearing components in aerospace structures, such as fuselage parts and landing-gear links [5].

Conventionally, TC21 is manufactured by forging, and the microstructure and mechanical properties of forged or laser additively manufactured TC21 have been investigated extensively [6–8]. Zhang et al. revealed the microstructural characteristics and the orientation-dependent anisotropic tensile behaviour of laser additively manufactured TC21 titanium alloy, and clarified the regulating effect of microstructural features such as grain-boundary α on the tensile properties and the fracture mechanisms along different directions [9]. Li et al. optimized the quasi-β forging parameters of TC21 titanium alloy so as to achieve precise control of its tri-modal microstructure, and established the correlation among the forging process, the tri-modal microstructure and the overall mechanical properties [6]. Chen et al. showed that the mechanical properties and the isotropy of quasi-β forged TC21 are dominated by boundary development and by dynamic lath precipitation [10]. Although TC21 forgings exhibit excellent mechanical properties, they still suffer from pronounced anisotropy, which impairs the stability of their mechanical response; in addition, the low material utilization and the high production cost of forging have severely restricted their wider application [11].

Powder metallurgy combined with hot isostatic pressing (PM-HIP) is a near-net-shape route in which the powder is densified under high temperature and high pressure, with an inert gas as the pressure-transmitting medium [12,13]. Because consolidation takes place under an isostatic stress state, the resulting components are fully dense, chemically homogeneous and free of macrosegregation, and their mechanical properties can be comparable to, or even better than, those of wrought titanium alloys [14,15]. The PM-HIP route also raises the material utilization from the 10–20% typical of forging to more than 50%, which is particularly attractive for an expensive metal such as titanium; for pre-alloyed spherical powder produced by the plasma rotating electrode process (PREP), HIP is the most common consolidation method [16].

The microstructure, and hence the mechanical properties, of PM-HIP titanium alloys depend sensitively on the HIP parameters. Zhang et al. showed that for powder Ti–6Al–4V the fine microstructure inherited from the powder coarsens as the HIP temperature or the holding time increases, and that the best balance of properties was obtained at 930 °C rather than at 880 or 1020 °C [17]. For powder-HIPped TA15, Zhu et al. reported that the microstructure changes from a basket-weave structure below 950 °C to a Widmanstätten structure above this temperature, accompanied by a decrease in both strength and elongation and by a change in the fracture mode from transgranular plastic fracture to mixed fracture involving intergranular cleavage [18]. These results indicate that the position of the HIP temperature relative to the β transus is the key parameter governing the microstructure of PM-HIP titanium alloys.

Heat treatment provides a further lever for tailoring the properties. In titanium alloys the fraction, morphology and distribution of the α and β phases critically determine the mechanical response [19–21], and solution and ageing treatments regulate the morphology of the α phase so as to achieve a better balance between strength and ductility [16,17]. For powder-HIPped TA15, Wang et al. showed that a solution and ageing treatment (930 °C/2 h/WQ + 600 °C/4 h/AC) improves the microstructural homogeneity and raises the room-temperature ultimate tensile strength from 907 to 1078 MPa through the precipitation of secondary α (α_s) within the β matrix [22]. The crystallographic aspects are equally important: the α phase precipitates from β according to the Burgers orientation relationship, $\{0001\}\alpha//\{110\}\beta$ and $\langle 11\text{–}20\rangle\alpha//\langle 111\rangle\beta$, and only a subset of the twelve crystallographically equivalent variants is usually selected, which controls the size of the α colonies and hence the effective slip length [23,24].

At present, most studies on TC21 deal with the microstructural evolution and property improvement under various forging conditions combined with heat treatment, whereas investigations on PM-HIP TC21—and in particular on the combined effect of the

HIP temperature and the subsequent heat treatment—remain scarce. In this study, TC21 titanium alloy was fabricated from PREP powder by HIP at temperatures spanning the β transus (890–1010 °C, 140 MPa/3 h) followed by a solution and ageing treatment (900 °C/1 h/AC + 590 °C/4 h/AC). The effect of the HIP temperature on the microstructure and on the room-temperature tensile properties was investigated systematically; the microstructural evolution and the α/β crystallographic orientation relationship were analysed, and the mechanism by which the HIP temperature controls the morphology, fraction and distribution of the α and β phases was elucidated. Particular attention is paid to the role of the α/β interfacial area and to the competition between the coarsening of the primary α and the interfacial strengthening provided by the secondary α. The results provide a theoretical basis and a technical reference for microstructure optimization and precise property control of PM-HIP TC21 titanium alloy.

2. Materials and Methods

2.1. Materials and Processing Technology

The TC21 titanium alloy powder used in this work was produced by the plasma rotating electrode process (PREP), as schematically illustrated in Figure 1. Atomisation was performed at a rotational speed of 24 000–26 000 rpm, an electrode current of 900–1100 A and a PV value of 36–38 mm, and the as-produced powder was sieved to a particle size range of 45–180 μm, which was used for the subsequent HIP experiments. The morphology and the cross-sectional microstructure of the as-prepared powder are presented in Figure 2. The chemical composition of the powder was determined by inductively coupled plasma optical emission spectrometry (ICP-OES), and the results are listed in Table 1. The cooling rate during PREP is of the order of 105–106 K/s according to previous measurements made within our research group, which is lower than that of gas atomisation. The microstructure of the powder is dominated by primary α phase, with a small amount of retained β phase distributed between the α phases. The primary α phase exhibits a morphology intermediate between dendritic and cellular, showing both cellular and short, thick dendritic features.

Table 1. TC21 titanium alloy powder composition (wt.%).

Sample	Al	Sn	Mo	Cr	Zr	Nb	Fe	C	N	H	O	Ti
TC21	6.28	2.12	2.75	1.58	2.12	1.91	0.022	0.005	0.007	0.0049	0.13	Bal

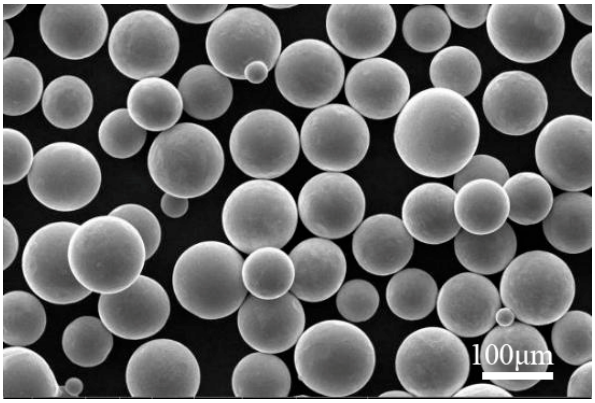


Figure 1. Microstructure of TC21 Powder.

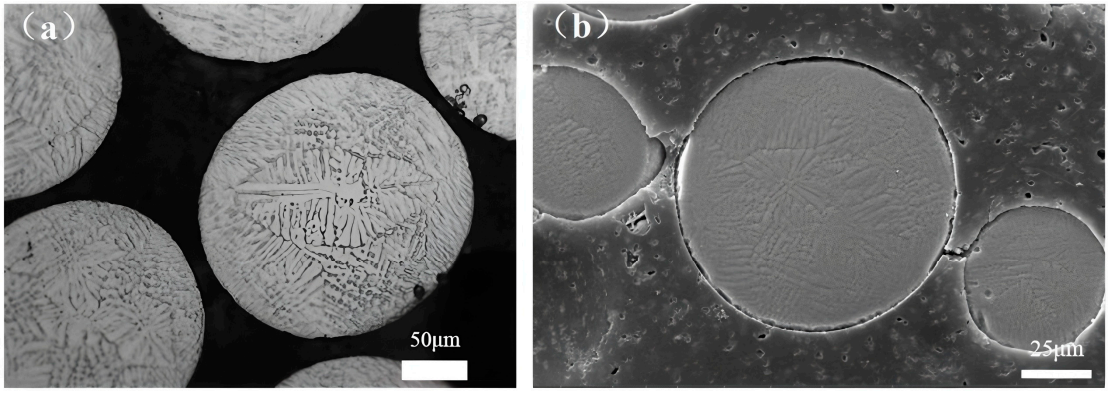


Figure 2. SEM micrographs of TC21 titanium alloy powder: (**a**) cross-sectional morphology of the powder particles; (**b**) magnified microstructure of a single powder particle.

The β-transus temperature (T_β) of the TC21 alloy was determined to be 970 ± 3 °C by metallographic observation in our group's earlier measurements on the same alloy system, and this value was adopted in the present study. Based on this value, five HIP temperatures were designed to span both the sub-transus (890 °C, 920 °C and 950 °C) and super-transus (980 °C and 1010 °C) groups, as shown in Figure 3a. TC21 alloy cylindrical billets with dimensions of φ100 mm × 650 mm were fabricated by HIP at each of these temperatures under 140 MPa for 3 h, with a heating rate of 5 °C/min and furnace cooling, using a QIH-286 hot isostatic press (Quintus, Västerås, Sweden) with high-purity argon (≥99.995%) as the pressure-transmitting medium. As illustrated in Figure 3b, all the five billets were subsequently subjected to the same two-step heat treatment, namely solution treatment at 900 °C for 1 h followed by aging at 590 °C for 4 h, both with air cooling, to achieve an optimal combination of strength and ductility.

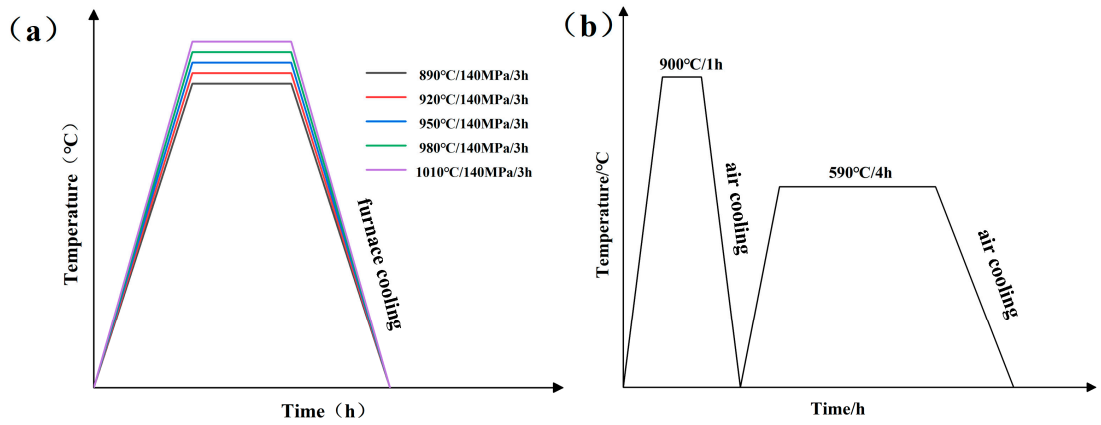


Figure 3. HIP and heat treatment schedules: (**a**) HIP at 890–1010 °C/140 MPa/3 h. (**b**) heat treatment at 900 °C/1 h air cooling and 590 °C/4 h air cooling.

2.2. Microstructure Characterization

All the specimens were cut from the mid-length section of the HIPed billets. For microstructural observation, the specimens were mounted, ground and polished, and then etched with Kroll's reagent ($V_{(HF)}$:$V_{(HNO3)}$:$V_{(H2O)}$ = 2:10:88) for approximately 20 s. Grinding was performed successively on water-cooled SiC abrasive papers of 200, 400, 800, 1200 and 2000 grit, and polishing was carried out with a 1.5 μm diamond suspension on a synthetic polishing cloth; the specimens were ultrasonically cleaned in ethanol and dried between the individual steps. The microstructure and the tensile fracture surfaces were examined using a field-emission scanning electron microscope (FE-SEM, JEOL JSM-7200F, JEOL Ltd., Tokyo, Japan) operated at an accelerating voltage of 15 kV. The size of the α

phase was measured from the SEM micrographs using Image-Pro Plus 6.0 image analysis software(Media Cybernetics, Inc., Rockville, MD ,USA).

X-ray diffraction (XRD) analysis was carried out on a Rigaku SmartLab SE diffractometer (Rigaku Cororation, Tokyo, Japan) with Cu Kα radiation operated at 40 kV and 40 mA, over a 2θ range of 30–80° at a scanning rate of 5°/min, in order to identify the phases present in the specimens after the heat treatment.

For EBSD analysis, the specimens were electrolytically polished after the mechanical grinding and polishing described above. The measurements were performed on a JSM-7900F field-emission SEM equipped with an EDAX Velocity Super detector, at an accelerating voltage of 20 kV and a step size of 0.2 μm; the data were analysed using OIM Analysis software (version 7.0; EDAX Inc., Mahwah, NJ, USA).

TEM specimens were mechanically ground to a thickness of about 50 μm, punched into discs 3 mm in diameter, and thinned by twin-jet electropolishing in a mixed solution of methanol and perchloric acid (9:1 by volume) at 20–25 V and 10–20 mA, with the electrolyte held at −30 to −25 °C; the thinned foils were finally cleaned by ion milling (Model 691, Gatan, Inc., Pleasanton, CA, USA). TEM observations and selected-area electron diffraction (SAED) were carried out on a Thermo Fisher Talos F200S microscope (Thermo Fisher Scientific Brno s.r.o., Brno, Czech Republic) operated at 200 kV, in order to examine the precipitated phases and the dislocation configuration and to determine their crystallographic characteristics.

Room-temperature tensile tests were conducted on round-bar specimens with M10 threaded ends (gauge diameter 10 mm, gauge length 50 mm) in accordance with GB/T 228.1-2021 [25], using a CMT5105 universal testing machine (MTS Systems, Eden Prairie, MN, USA) at a crosshead speed of 1 mm/min. Three specimens were tested for each condition; the average values are reported together with the standard deviation (Tables 2 and 3), which documents the repeatability of the tensile tests. All processing and instrument parameters reported in Section 2 (temperatures, pressures, voltages, currents and scanning rates) are nominal set values, which were controlled within the calibration tolerances of the corresponding equipment.

Table 2. Tensile properties and characteristic microstructural parameters of the TC21 alloys HIPed at different temperatures (140 MPa/3 h).

Hot Isostatic Pressing Parameters	YS (MPa)	UTS (MPa)	A (%)	Z (%)
890 °C/140 MPa/3 h	1032 ± 2.8	1133 ± 4.2	10.5 ± 1.4	29 ± 1.4
920 °C/140 MPa/3 h	1004.5 ± 0.7	1106.5 ± 6.4	11 ± 1.4	29.5 ± 9.2
950 °C/140 MPa/3 h	980 ± 0.7	1077 ± 4.9	17 ± 0.7	36 ± 6.4
980 °C/140 MPa/3 h	949.5 ± 4.9	1038 ± 4.2	18.25 ± 0.4	52 ± 1.4
1010 °C/140 MPa/3 h	908.5 ± 4.9	1039 ± 9.9	9.75 ± 1.8	20 ± 1.4

Table 3. Tensile properties and characteristic microstructural parameters of the TC21 alloys HIPed at different temperatures (140 MPa/3 h) and subsequently heat-treated at 900 °C/1 h/air cooling + 590 °C/4 h/air cooling.

Hot Isostatic Pressing Parameters	YS (MPa)	UTS (MPa)	A (%)	Z (%)	dα_p (μm)	dα_s (μm)
890 °C/140 MPa/3 h	1180 ± 1.4	1238.5 ± 2.1	8.75 ± 1.76	16.5 ± 2.31	8.4 ± 1.31	0.07 ± 0.01
920 °C/140 MPa/3 h	1186 ± 4.9	1247.5 ± 4.5	10.75 ± 2.47	24 ± 3.11	11.2 ± 2.05	0.08 ± 0.03
950 °C/140 MPa/3 h	1195.5 ± 3.5	1259.5 ± 3.63	13 ± 2.82	35.5 ± 2.12	11.9 ± 1.66	0.1 ± 0.05
980 °C/140 MPa/3 h	1211 ± 14.1	1278.5 ± 10.6	8.75 ± 1.76	29.5 ± 4.94	15.7 ± 2.53	0.13 ± 0.06
1010 °C/140 MPa/3 h	1126 ± 9.9	1201 ± 9.5	4 ± 1.41	9.5 ± 0.7	20.7 ± 2.12	0.17 ± 0.04

3. Results

3.1. SEM Microstructures of Hot Isostatically Pressed (HIPed) TC21 Titanium Alloy

Figure 4 shows the SEM micrographs of TC21 titanium alloy under different HIP temperatures. As shown in Figure 4a, when the HIP temperature was 890 °C (140 MPa/3 h), the microstructure of TC21 consisted of primary α (α_P), lamellar α (α_L), and β phases. The αL phase exhibited a fine lamellar structure and was uniformly distributed within the matrix, the α_P phase appeared as fine equiaxed grains, and the β phase existed as a continuous network or block. The overall grain size was small and relatively homogeneous. As shown in Figure 4b, when the HIP temperature was increased to 920 °C, the microstructure was still composed of α_P, α_L, and β phases, but grain coarsening began to occur. As quantitatively revealed in Figure 4g, the mean equivalent diameter of the equiaxed α phase increased from 8.51 ± 0.31 μm at 890 °C to 9.71 ± 0.27 μm at 920 °C (+14.1%), indicating the onset of coarsening. The interlamellar spacing of the α_L phase increased slightly, the size of the α_L phase became larger, and the continuity of the β phase was enhanced. The uniformity of the overall microstructure was lower than that at 890 °C (140 MPa/3 h). As shown in Figure 4c, when the HIP temperature reached 950 °C (140 MPa/3 h), the α phase gradually became equiaxed. The originally fine lamellar α_L phase spheroidized and transformed into approximately circular or elliptical equiaxed grains, while the β phase was significantly coarsened, showing a large blocky or dendritic morphology. As shown in Figure 4d, at a HIP temperature of 980 °C (140 MPa/3 h), the microstructure was mainly composed of equiaxed α phase, a small proportion of lamellar α phase, and β phase. The grain size increased, and equiaxed α_P became dominant. Lamellar α_L phase remained only in some regions, and the β phase further grew and interconnected, forming a relatively coarse β matrix. This transformation occurred in two stages: First, the lamellar boundaries split due to the reduction of dislocation substructures and the decrease in interfacial energy, dividing the continuous lamellar α phase into smaller units. Second, boundary migration and Ostwald ripening promoted the evolution of lamellar α phase into equiaxed α phase [26,27]. As shown in Figure 4e,f, when the HIP temperature was 1010 °C (140 MPa/3 h), which exceeded the β-transus temperature, the TC21 sample exhibited a microstructure with interlocking α colonies and basket-weave morphology, typical of a Widmanstätten structure. This was because all α phases transformed into β phase during HIP, and during subsequent cooling, α phase re-precipitated along the β grain boundaries, forming the observed α colonies distributed along grain boundaries. These colonies interlocked with each other and formed a basket-weave structure together with the β matrix. The α colonies in the structure were large and regularly shaped, while the β phase appeared as a coarse basket-weave framework.

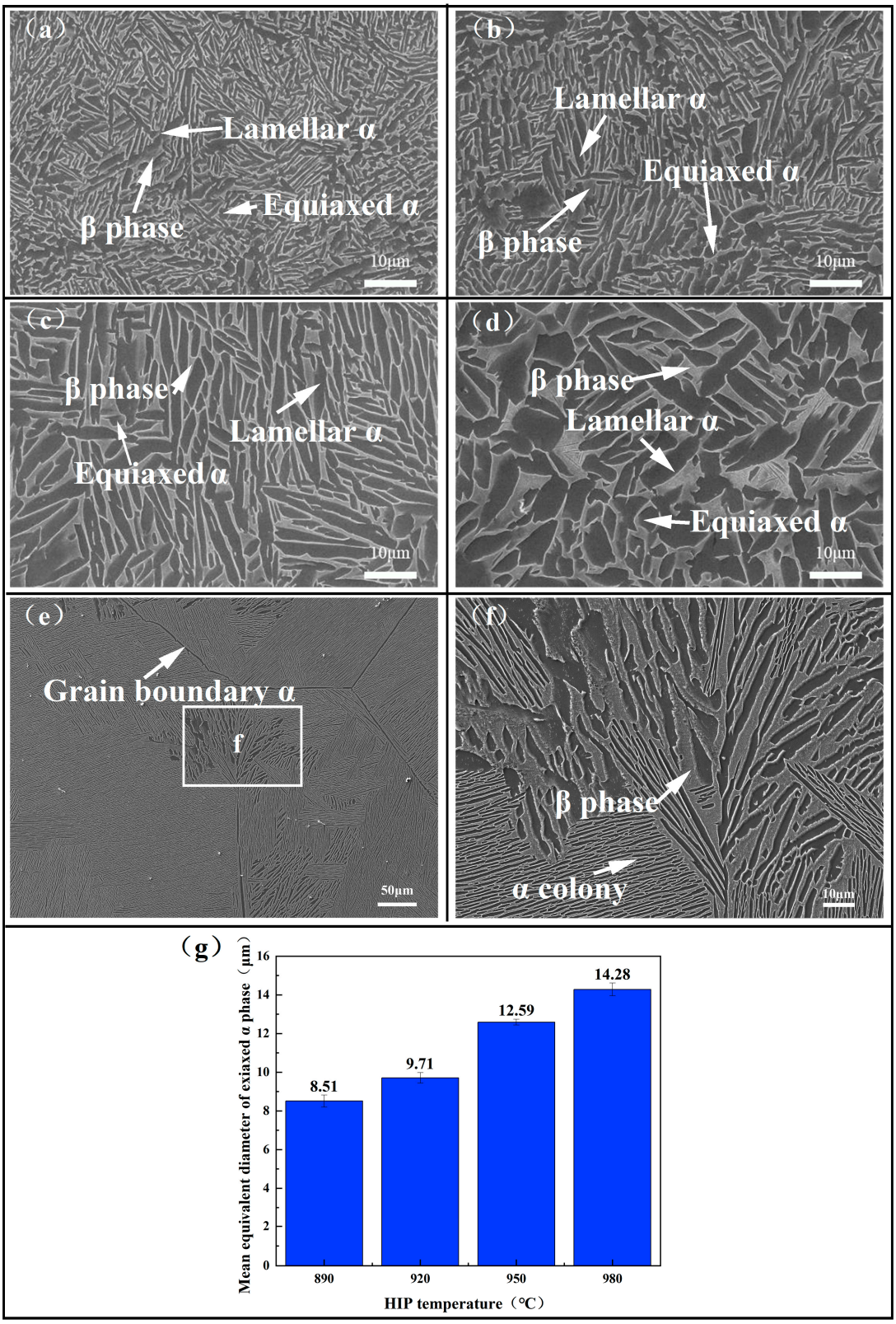


Figure 4. SEM microstructures of TC21 titanium alloy at different HIP temperatures (**a**) 890 °C/140 MPa/3 h; (**b**) 920 °C/140 MPa/3 h; (**c**) 950 °C/140 MPa/3 h; (**d**) 980 °C/140 MPa/3 h; (**e**,**f**) 1010 °C/140 MPa/3 h; (**g**) α phase size at 890–980 °C (HIP: 140 MPa, 3 h).

3.2. SEM Microstructure of TC21 After Hot Isostatic Pressing and Subsequent Heat Treatment

Figure 5 shows the microstructures of TC21 titanium alloy after the same solution and aging treatment at different HIP temperatures. The microstructure of TC21 alloy evolves regularly and continuously with increasing HIP temperature. As shown in Figure

5a,b, the microstructure of the sample HIPed at 890 °C mainly consists of fine and uniform lamellar α phase and equiaxed α phase, with fine lamellar β phase dispersedly distributed among them. A large number of fine secondary α (α_s) precipitates exist in the β phase. The α phase exhibits regular morphology, small size and uniform distribution, with no obvious grain boundary α phase. As shown in Figure 5c–f, when the temperature increases to 920 °C and 950 °C, the volume fraction of α phase gradually decreases, the phase size is slightly coarsened, and the proportion and distribution range of lamellar α phase increase significantly. The microstructure gradually transitions from a bimodal structure dominated by equiaxed α phase to a basket-weave structure with higher lamellar content. Fine discontinuous grain boundary α phase can be observed in local regions, without forming a continuous coating structure. When the HIP temperature rises to 980 °C near the β-transus temperature, only a small amount of isolated equiaxed α phase remains in the microstructure. The microstructure is dominated by uniformly interlaced and densely arranged basket-weave lamellar α phase with fine size and random orientation. The grain boundary α phase is distributed as discontinuous dots without a continuous network, and the microstructure uniformity reaches the optimum. As shown in Figure 5i,j, when the temperature further increases to 1010 °C in the single β phase region, equiaxed α phase disappears completely. Clear coarse prior β grain boundaries can be observed, and a continuous and complete network of grain boundary α phase precipitates at the grain boundaries. Inside the grains, coarse α colonies with single orientation and typical Widmanstätten lamellar structure are formed. The lamellar phases are regularly arranged with obvious directionality, and the microstructure uniformity decreases significantly, showing obvious overheating and coarsening characteristics in the single β phase region.

3.3. XRD Patterns of As-HIP TC21 After Heat Treatment

Figure 6 shows the XRD patterns of the TC21 specimens after HIP at 890, 920, 950, 980 and 1010 °C (140 MPa, 3 h) followed by heat treatment (900 °C/1 h/air cooling + 590 °C/4 h/air cooling). All patterns are dominated by hexagonal α-Ti (JCPDS No. 44-1294) and contain weak reflections of BCC β-Ti (JCPDS No. 44-1288); no α″ martensite, hydrides or other second phases are detected. The strongest α-Ti reflections—(002) at ~38.4°, (101) at ~40.3°, (102) at ~53.0°, (110) at ~63.1°, (103) at ~70.8° and (112) at ~76.5°—are clearly indexed, while the β (110), (200) and (211) reflections appear at ~38.6°, ~55.6° and ~74.6°. The α (002) and β (110) peaks overlap near 38–39°, so the β (200) reflection is used as an isolated indicator of the β phase.

The α (101) peak is the most intense in every specimen, confirming an α-rich microstructure after ageing. The β (200) peak is barely above the background for the 890–980 °C samples ($I\beta(200)/I\alpha(101) \approx 0.018$–$0.030$) and is better resolved at 1010 °C (≈ 0.10, and shifted to ≈ 56.3°). It should be emphasised that these weak β reflections do not permit a quantitative estimate of the retained-β fraction: at this level the β (200) peak overlaps the tail of the α (002) and α (101) reflections and its intensity is extremely sensitive to the composition, the lattice parameter and the residual stress of the retained β, so that the XRD is used here only to identify the phases present (α + β, with no α″, hydrides or other second phases). The quantitative β fractions are instead taken from the EBSD area fractions reported in Section 3.4. The clearer β (200) reflection at 1010 °C therefore indicates a change in the composition or the lattice parameter of the retained β—for example, a higher content of β-stabilising elements, or the relief of transformation strain—rather than a higher β volume fraction, which is in fact the lowest of the five conditions.

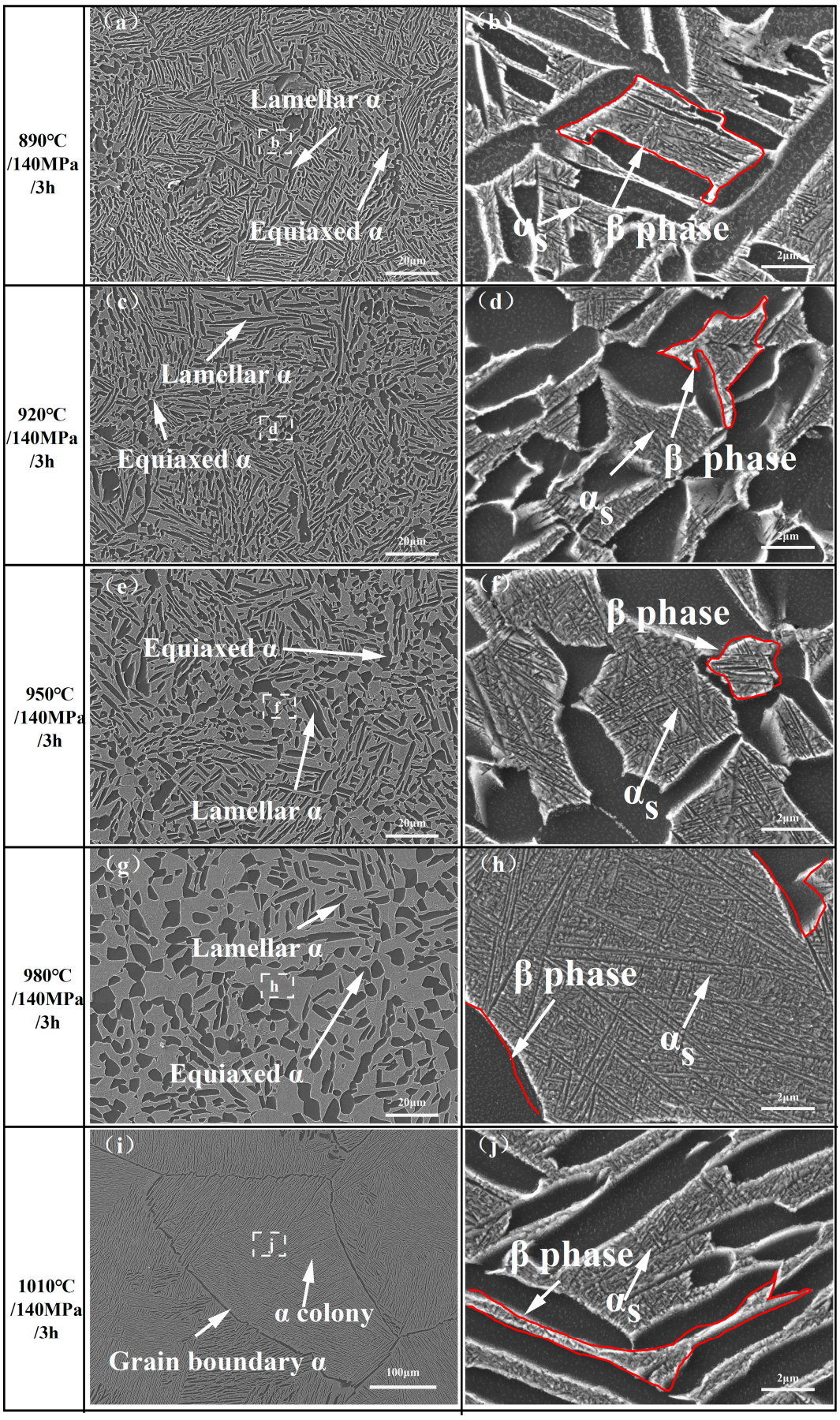


Figure 5. Microstructures of TC21 alloy after HIP at different temperatures followed by heat treatment (900 °C/1 h, air cooling + 590 °C/4 h, air cooling): (**a**,**b**) 890 °C/140 MPa/3 h; (**c**,**d**) 920 °C/140 MPa/3 h; (**e**,**f**) 950 °C/140 MPa/3 h; (**g**,**h**) 980 °C/140 MPa/3 h; (**i**,**j**) 1010 °C/140 MPa/3 h.

https://doi.org/10.3390/met16101111

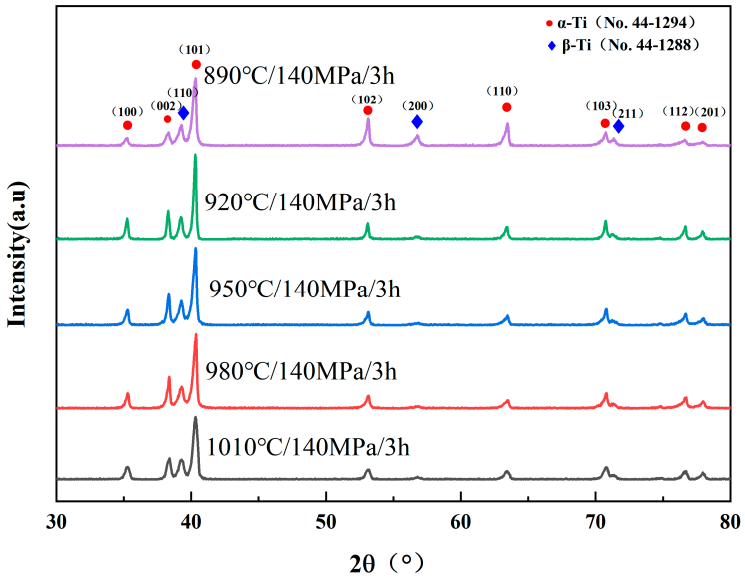


Figure 6. XRD patterns of TC21 alloy after HIP (890–1010 °C/140 MPa/3 h) and heat treatment (900 °C/1 h, air cooling + 590 °C/4 h, air cooling).

3.4. EBSD Map of Heat-Treated TC21 Alloy

Figure 7 shows the EBSD results of the TC21 alloy HIPed at 890 °C/140 MPa for 3 h and subsequently heat-treated at 900 °C/1 h/air cooling + 590 °C/4 h/air cooling. The inverse pole figure (IPF) map in Figure 7a (Z0 direction) shows equiaxed and lamellar α phases with various orientations distributed in the retained β matrix, and the orientation colours are rather uniformly distributed in the standard triangle, indicating no pronounced texture or directionality. The corresponding phase map (Figure 7b) gives area fractions of 81% α and 19% β, which is consistent with the fact that both the HIP and the solution treatment were performed below the β transus. The grain size distribution of the α phase (Figure 7e) is slightly right-skewed, with a mean size of 8.4 μm), suggesting that the fine equiaxed α formed by globularisation during the sub-transus HIP exposure.

Two regions containing α lamellae with different orientations were selected (Regions I and II, Figure 7c,d), and the corresponding pole figures were reconstructed (Figure 7f,g). In Region I, (000-1)α1//(011)β1, (000-1)α2//(110)β1 and (0001)α3//(-101)β1, together with [2-1-10]α1/α3//[1-11]β1; the α variants in Region II obey the same relationship with the β matrix. These results confirm that the α phase follows the Burgers orientation relationship with the β matrix, namely {0001}α//{110}β and <11-20>α//<111>β. Although twelve crystallographically equivalent variants are possible within one β grain, only three were detected in each of the two regions examined, which is a local observation restricted to the regions analysed and does not by itself demonstrate variant selection; the paired α1/α3 variants share the same close-packed direction but align different {0001}/{110} planes, corresponding to the low-energy 10.5°/[0001] relationship reported for Burgers variant pairs [24], which therefore lowers the α/α interfacial energy. The weak texture observed in the regions examined, together with the fine equiaxed α, indicates that the HIPed alloy possesses a homogeneous and nearly isotropic microstructure.

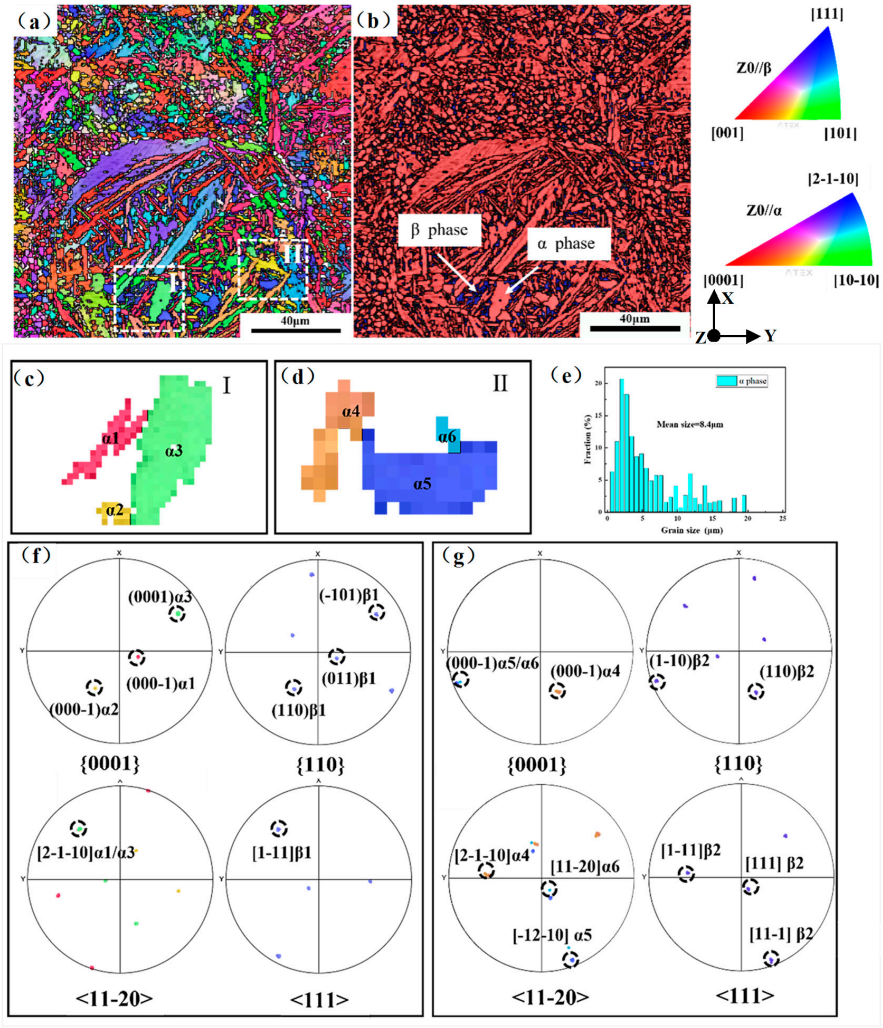


Figure 7. EBSD analysis of the TC21 titanium alloy after HIP at 890 °C/140 MPa for 3 h and subsequent heat treatment (900 °C/1 h/air cooling + 590 °C/4 h/air cooling): (**a**) inverse pole figure (IPF) map along the Z0 direction; (**b**) phase distribution map; (**c**,**d**) selected regions I and II containing α lamellae with different orientations; (**e**) grain size distribution of the α phase; (**f**,**g**) pole figures showing the orientation relationship between the α and β phases in regions I and II, respectively.

Figure 8 shows the EBSD results of the TC21 alloy HIPed at 920 °C/140 MPa for 3 h and subsequently heat-treated at 900 °C/1 h/AC + 590 °C/4 h/AC. The inverse pole figure (IPF) map in Figure 8a (Z0 direction) again shows equiaxed and lamellar α phases with various orientations distributed in the retained β matrix, without pronounced texture or directionality. The phase map (Figure 8b) gives area fractions of 79% α and 21% β; compared with the alloy HIPed at 890 °C (Figure 7), the α fraction decreases slightly while the retained β increases, which is consistent with the equilibrium β fraction increasing as the HIP temperature approaches the β transus. The grain size distribution of the α phase (Figure 8e) is slightly right-skewed, with a mean size of 11.2 ± 2.05 μm. The coarser equiaxed α relative to the 890 °C sample (8.4 μm, Figure 7e) indicates that the higher HIP temperature promotes α growth and weakens the driving force for globularisation. Figure 8c,d present two regions selected within a single β grain (Regions I and II), in which several α lamellae of clearly different crystallographic orientations (labelled α1–α6) coexist; this further confirms that multiple α orientations are distributed in a nearly random manner inside one β grain, in accordance with the weak texture noted above.

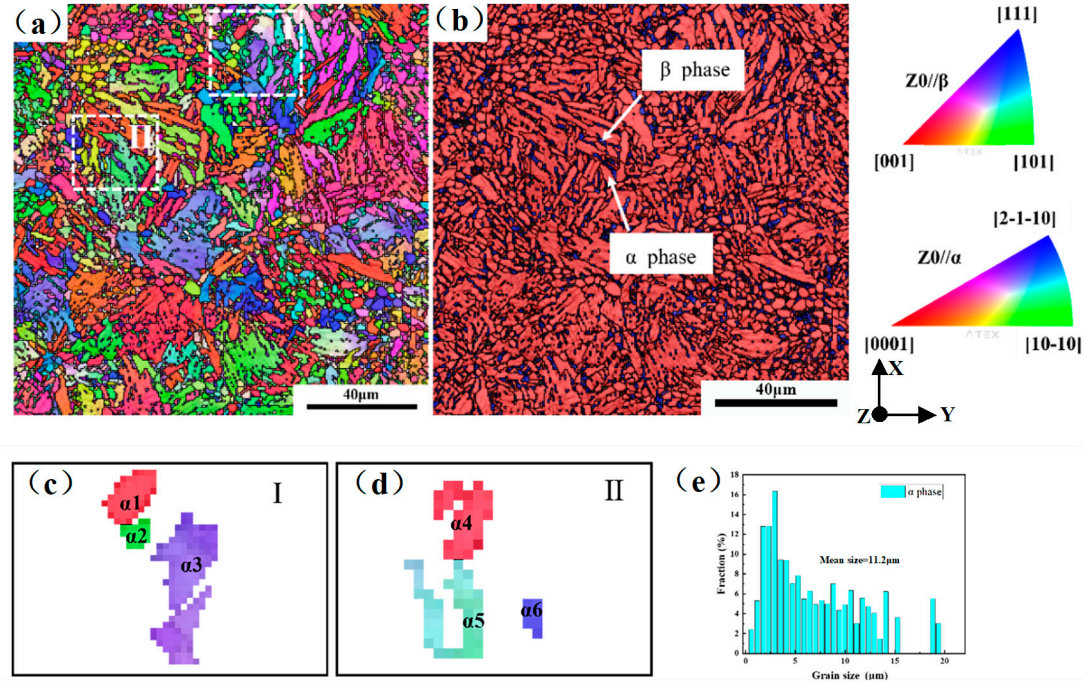


Figure 8. EBSD analysis of the TC21 titanium alloy after HIP at 920 °C/140 MPa for 3 h and subsequent heat treatment (900 °C/1 h/air cooling + 590 °C/4 h/air cooling): (**a**) inverse pole figure (IPF) map along the Z0 direction; (**b**) phase distribution map; (**c**,**d**) selected regions I and II within a single β grain, showing α lamellae of different orientations (α1–α6); (**e**) grain size distribution of the α phase.

Figure 9 shows the EBSD results of the TC21 alloy HIPed at 950 °C/140 MPa for 3 h and subsequently heat-treated at 900 °C/1 h/air cooling + 590 °C/4 h/air cooling. The inverse pole figure (IPF) map in Figure 9a (Z0 direction) again shows equiaxed and lamellar α phases with various orientations distributed in the retained β matrix, without pronounced texture or directionality. The phase map (Figure 9b) gives area fractions of 74% α and 26% β. Together with Figures 7 and 8, the α fraction measured at room temperature decreases monotonically with increasing HIP temperature (81% → 79% → 74%), while the retained β increases correspondingly (19% → 21% → 26%); this is consistent with a lower fraction of primary α and a more stable retained β as the HIP temperature approaches the measured β transus of 970 ± 3 °C, the 950 °C condition being only about 20 °C below it. The grain size distribution of the α phase (Figure 9e) is slightly right-skewed, with a mean size of 11.9 ± 1.66 μm; combined with the values of 8.4 ± 1.31 μm (890 °C) and 11.2 ± 2.05 μm (920 °C), the α grains coarsen progressively with increasing HIP temperature, although the coarsening slows down above 920 °C. Figure 9c,d present two regions selected within a single β grain (Regions I and II), in which several α lamellae of clearly different crystallographic orientations (labelled α1–α6) coexist, again confirming the nearly random distribution of α orientations within one β grain.

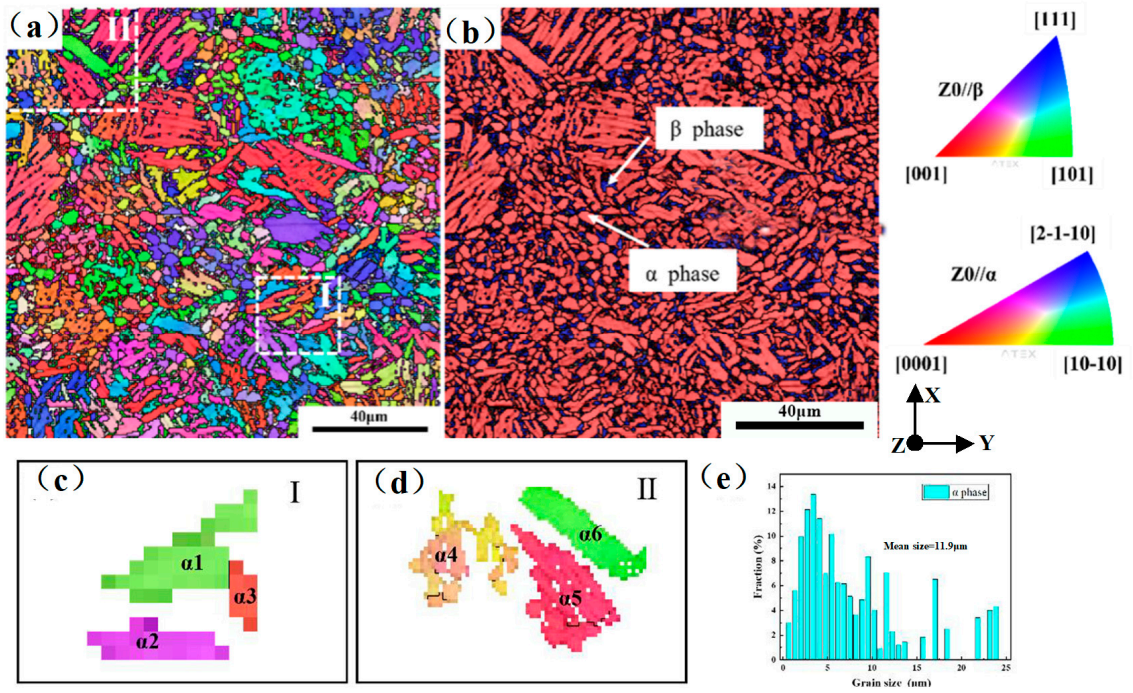


Figure 9. EBSD analysis of the TC21 titanium alloy after HIP at 950 °C/140 MPa for 3 h and subsequent heat treatment (900 °C/1 h/air cooling + 590 °C/4 h/air cooling): (**a**) inverse pole figure (IPF) map along the Z0 direction; (**b**) phase distribution map; (**c**,**d**) selected regions I and II within a single β grain, showing α lamellae of different orientations (α1–α6); (**e**) grain size distribution of the α phase.

Figure 10 shows the EBSD results of the TC21 alloy HIPed at 980 °C/140 MPa for 3 h and subsequently heat-treated at 900 °C/1 h/air cooling + 590 °C/4 h/air cooling. It should be noted that 980 °C lies about 10 °C above the measured β transus of 970 ± 3 °C, so that the alloy was fully β during the HIP stage; the microstructure presented here was therefore developed during the subsequent solution treatment, cooling and ageing, rather than being inherited from globularised primary α as in the sub-transus HIP conditions. The inverse pole figure (IPF) map in Figure 10a (Z0 direction) shows a microstructure dominated by basket-weave lamellar α, in which the lamellae are uniformly interlaced, densely arranged and nearly randomly oriented, together with a small amount of isolated equiaxed α, all distributed in the retained β matrix, without pronounced texture or directionality. The phase map (Figure 10b) gives area fractions of 80% α and 20% β. In contrast to the sub-transus HIP conditions (Figures 7–9), where the room-temperature α fraction decreased monotonically with increasing HIP temperature (81% → 79% → 74%), the α fraction increases to 80% and the mean α grain size rises to 15.7 ± 2.53 μm (Figure 10e). This reversal indicates a change in mechanism: above the β transus, the primary α is completely dissolved during HIP, and the amount and morphology of the α phase in the final microstructure are controlled by the precipitation of α from the β matrix during cooling and the subsequent heat treatment, yielding a coarse basket-weave α structure instead of the fine globularised primary α obtained below the transus. Figure 10c,d present two regions selected within the prior β grain (Regions I and II), in which α with clearly different crystallographic orientations (labelled α1–α3) coexists, again indicating a nearly random orientation distribution, in agreement with the basket-weave morphology and the discontinuous grain-boundary α observed by SEM (Figure 5i,j).

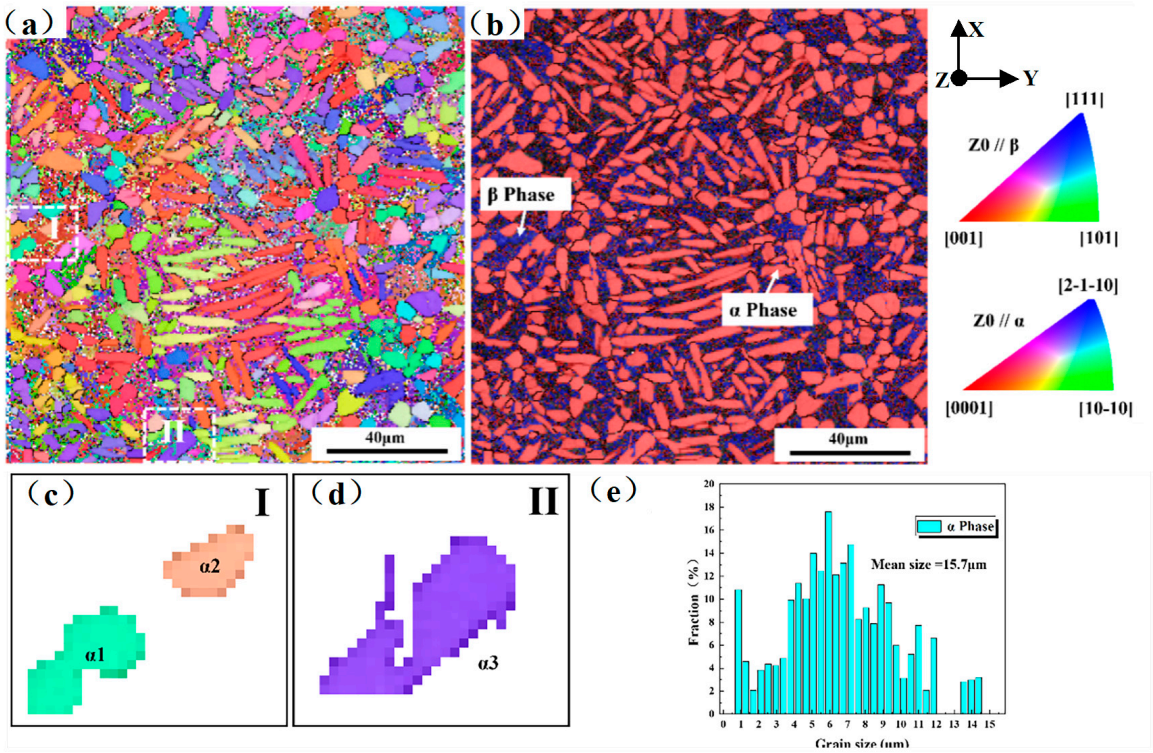


Figure 10. EBSD analysis of the TC21 titanium alloy after HIP at 980 °C/140 MPa for 3 h and subsequent heat treatment (900 °C/1 h/air cooling + 590 °C/4 h/air cooling): (**a**) inverse pole figure (IPF) map along the Z0 direction; (**b**) phase distribution map; (**c**,**d**) selected regions I and II showing α with different orientations (α1–α3); (**e**) grain size distribution of the α phase.

Figure 11 shows the EBSD results of the TC21 alloy HIPed at 1010 °C/140 MPa for 3 h, i.e., about 40 °C above the measured β transus of 970 ± 3 °C, followed by the same heat treatment (900 °C/1 h/air cooling + 590 °C/4 h/air cooling). The inverse pole figure (IPF) map in Figure 11a (Z0 direction) shows lamellar α colonies with various orientations distributed within the coarse prior β grains, without pronounced macro-texture. The phase map (Figure 11b) gives area fractions of 90% α and 10% β. No equiaxed primary α is detected, confirming that the primary α inherited from the powder was completely dissolved at this HIP temperature and that the entire α phase in the final microstructure precipitated from the β matrix during cooling and the subsequent heat treatment. The grain size distribution of the α phase (Figure 11e) gives a mean size of 20.7 ± 2.12 μm. Combined with the value of 15.7 ± 2.53 μm obtained at 980 °C (Figure 10e), the α feature size coarsens further with increasing superheating above the transus, which is attributed to the growth of the prior β grains and the correspondingly coarser α colonies formed within them. Figure 11c,d present two selected α regions (α1 and α2) with different orientations, again indicating a nearly random orientation distribution of the α phase.

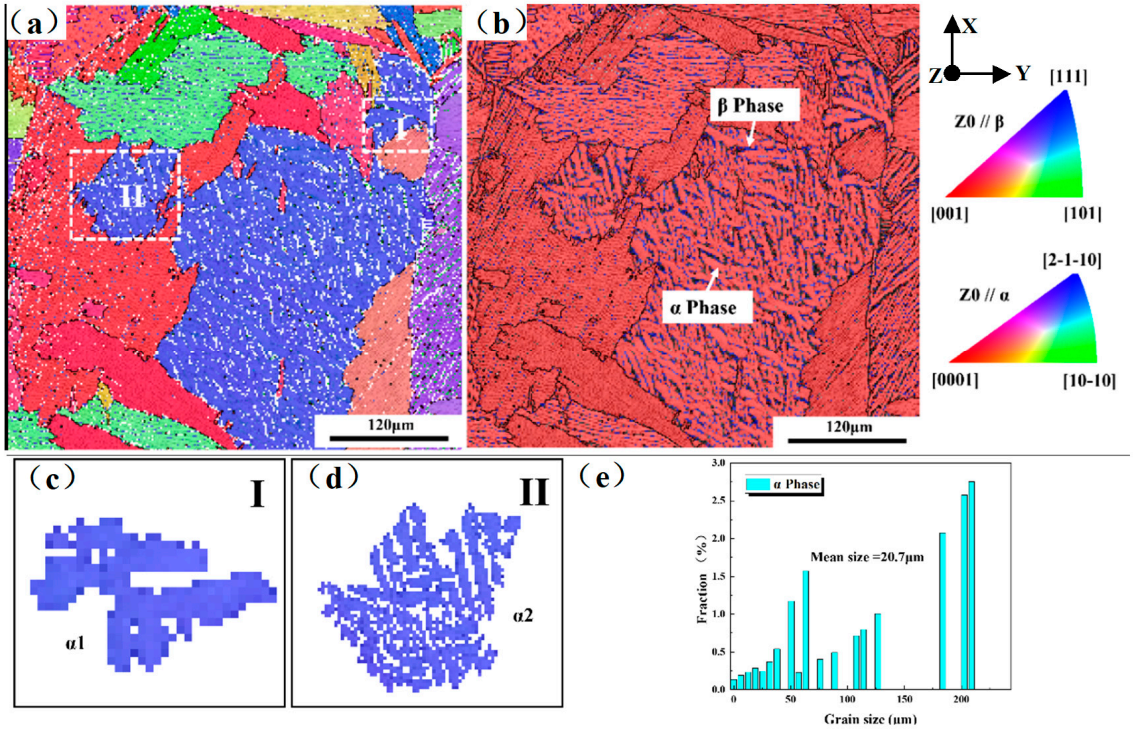


Figure 11. EBSD analysis of the TC21 titanium alloy after HIP at 1010 °C/140 MPa for 3 h and subsequent heat treatment (900 °C/1 h/air cooling + 590 °C/4 h/air cooling): (**a**) inverse pole figure (IPF) map along the Z0 direction; (**b**) phase distribution map; (**c**,**d**) selected regions I and II showing α with different orientations (α1, α2); (**e**) grain size distribution of the α phase.

3.5. TEM Microstructure of TC21 Alloy After Heat Treatment

Figure 12 shows TEM images of the heat-treated TC21 alloy HIPed at 890 °C. Under bright-field imaging, densely distributed secondary α (α_s) phases are observed (Figure 12a–c), together with a small amount of lamellar α (α_L) with a thickness of 0.1–0.5 μm (Figure 12d). The identification of the α precipitates is based on diffraction evidence. First, the SAED pattern acquired from an α_s/β region (inset in Figure 12e) was indexed: the reflections of the hcp α and the bcc β were identified, and the pattern corresponds to the β//α zone axis, on which {0001}α//{110}β and <11-20>α//<111>β are directly revealed, confirming that the precipitates and the matrix obey the Burgers orientation relationship. Second, dark-field images were formed using the indexed α reflections for the three α_s variants (Figure 12f–h); in each case only the α_s precipitates are imaged while the β matrix remains dark, which verifies that the labelled particles are α phase. This is consistent with the α/β Burgers orientation relationship established by EBSD for the same heat-treatment condition (Figure 7f,g), confirming that the α_s precipitates formed from the retained β during cooling and ageing. A large number of α_s precipitates are distributed in the β matrix (Figure 12e); the <11-20> direction of α_s is parallel to <111> of β, and the {0001} plane of α_s is parallel to {110} of the β matrix. The three α_s variants exhibit essentially uniform size and morphology, with a length of 0.14–0.44 μm and an average thickness of 0.07 ± 0.01 μm.

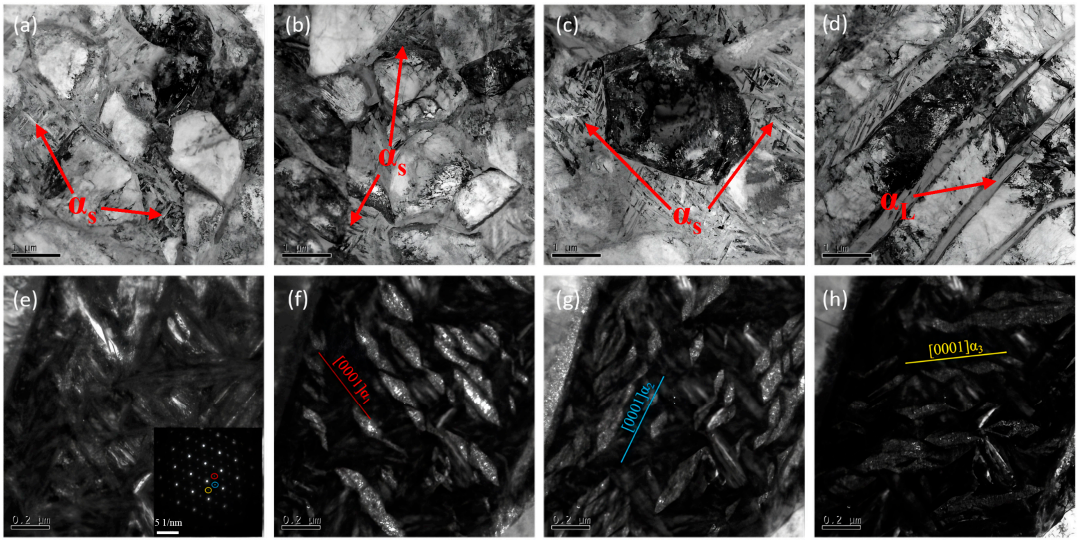


Figure 12. TEM analysis of the TC21 alloy after HIP at 890 °C/140 MPa for 3 h and subsequent heat treatment (900 °C/1 h/air cooling + 590 °C/4 h/air cooling): (**a**–**c**) bright-field (BF) images of needle-like secondary α (α_s) in the β matrix; (**d**) BF image of lamellar α (α_L) with thin films of retained β between the laths; (**e**) BF image with the inset SAED pattern recorded along the [111]β/[$2\bar{1}\bar{1}0$]α zone axes; (**f**–**h**) dark-field (DF) images of three α_s variants.

Figure 13 shows TEM images of the TC21 alloy HIPed at 920 °C/140 MPa for 3 h and heat-treated at 900 °C/1 h/air cooling + 590 °C/4 h/air cooling. Needle-like secondary α (α_s) is densely distributed (Figure 13a), similar to the 890 °C condition but coarser, and long rod-like lamellar α (α_L) is also present, with an average thickness of 1.2 ± 0.3 μm (Figure 13b). Twin lamellae are observed adjacent to the β matrix, containing a high density of stacking faults (Figure 13c). The SAED pattern taken from this region (Figure 13d) shows two sets of α reflections related by a mirror operation, confirming that the lamellae are {10-11} type twins. Figure 13e shows a large number of α_s precipitates in the β matrix; the inset SAED pattern confirms the Burgers orientation relationship between α_s and β. <$2\bar{1}\bar{1}0$>α_s//<111>β and {0001}α_s//{110}β. Dark-field images of the three α_s variants, formed with the α reflections circled in Figure 13e, are shown in Figure 13f–h (g = {10-10}α1, {0001}α2 and {0001}α3, respectively). The α_s variants are essentially uniform in size and morphology, with lengths of 0.3–0.6 μm and an average thickness of 0.08 ± 0.03 μm.

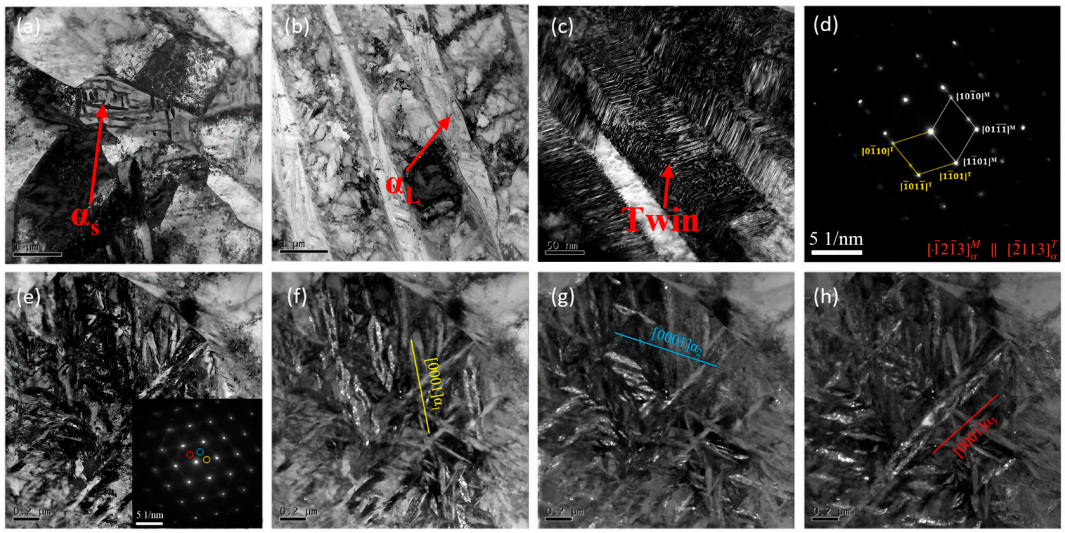


Figure 13. TEM analysis of the TC21 alloy after HIP at 920 °C/140 MPa for 3 h and subsequent heat treatment (900 °C/1 h/air cooling + 590 °C/4 h/air cooling): (**a**) BF image of needle-like α_s in the β

matrix; (**b**) BF image of rod-like α_L; (**c**) BF image of {10-11} twin lamellae containing a high density of stacking faults; (**d**) SAED pattern taken from (**c**), showing mirror-symmetric twin reflections; (**e**) image of α_s in the β matrix with the inset SAED pattern along the [111]β/[$2\bar{1}\bar{1}0$]α zone axes, corresponding to the Burgers orientation relationship; (**f–h**) DF images of three α_s variants formed with g = {10-10}α1, {0001}α2 and {0001}α3, respectively.

Figure 14 shows TEM images of the TC21 alloy HIPed at 950 °C/140 MPa for 3 h and heat-treated at 900 °C/1 h/air cooling + 590 °C/4 h/air cooling. Coarse lamellar α (α_L) with a long rod-like morphology and an average thickness of 1.7 μm is shown in Figure 14a. A large number of needle-like secondary α (α_s) precipitates are distributed in the β matrix between the α_L laths (Figure 14b–d), with lengths of 0.4–4.3 μm as measured from Figure 14a–d. The SAED pattern (inset in Figure 14e) confirms the Burgers orientation relationship between α_s and β, i.e., <$2\bar{1}\bar{1}0$>α_s//<111>β and {0001}α_s//{110}β. Dark-field images of the three α_s variants, formed with the reflections circled in Figure 14e, are shown in Figure 14f–h (g = (0001)α1, (0001)α2 and (0001)α3, respectively. The α_s variants are essentially uniform in size and morphology, with lengths of 0.3–1.5 μm and an average thickness of 0.1 ± 0.05 μm.

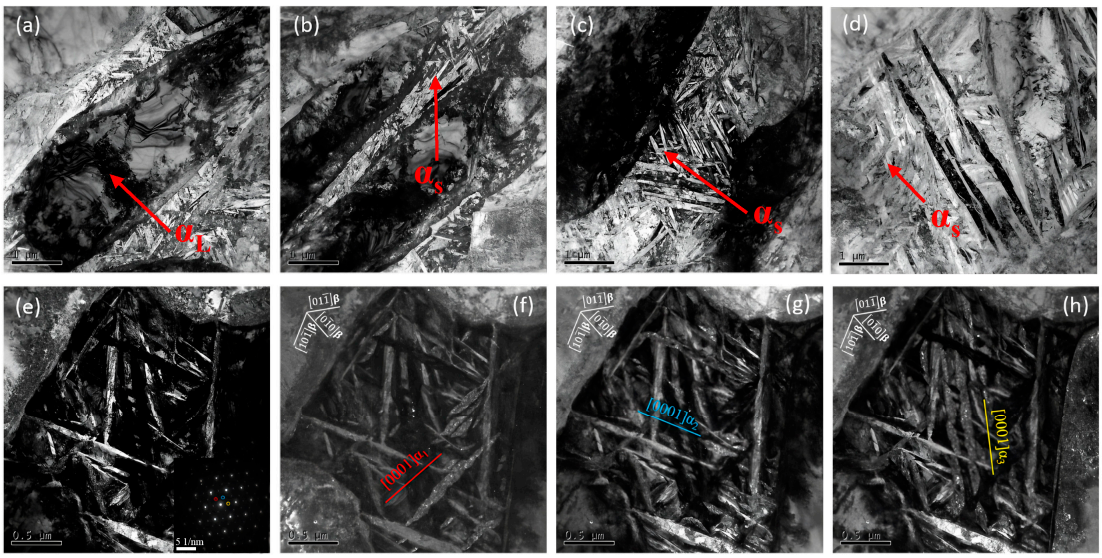


Figure 14. TEM analysis of the TC21 alloy after HIP at 950 °C/140 MPa for 3 h and subsequent heat treatment (900 °C/1 h/air cooling + 590 °C/4 h/air cooling): (**a**) BF image of coarse rod-like α_L; (**b–d**) BF images of needle-like α_s in the β matrix between the α_L laths; (**e**) DF image with the inset SAED pattern recorded along the [111]β/[$2\bar{1}\bar{1}0$]α zone axes; (**f–h**) DF images of three α_s variants formed with g = (0001)α1, (0001)α2 and (0001)α3, respectively.

Figure 15 shows TEM images of the TC21 alloy HIPed at 980 °C/140 MPa for 3 h, i.e., slightly above the measured β transus of 970 ± 3 °C, followed by heat treatment at 900 °C/1 h/air cooling + 590 °C/4 h/air cooling. A small amount of coarse equiaxed α (α_p) with a diameter of approximately 6 μm is surrounded by the β matrix (Figure 15a); since 980 °C lies above the β transus, this α precipitated from the β matrix during subsequent cooling and ageing rather than being primary α inherited from the sub-transus conditions. A large number of needle-like secondary α (α_s) precipitates with lengths of 0.3–7.0 μm are distributed in the β matrix (Figure 15b–d). The SAED pattern (inset in Figure 15e) confirms the Burgers orientation relationship between α_s and β. <$2\bar{1}\bar{1}0$>α_s//<111>β and {0001}α_s//{110}β. Owing to the symmetry of this orientation relationship, three α_s variants coexist, related by successive 60° rotations about the common <$2\bar{1}\bar{1}0$>α_s//<111>β axis (Figure 15f–h). The

dark-field images, formed with g = (0001)α1, (0001)α2 and (0001)α3, respectively (reflections circled in Figure 15e), confirm the three variants and show that the long axes of the needle-like α_s lie within their {0001} basal planes along <11-20>α_s

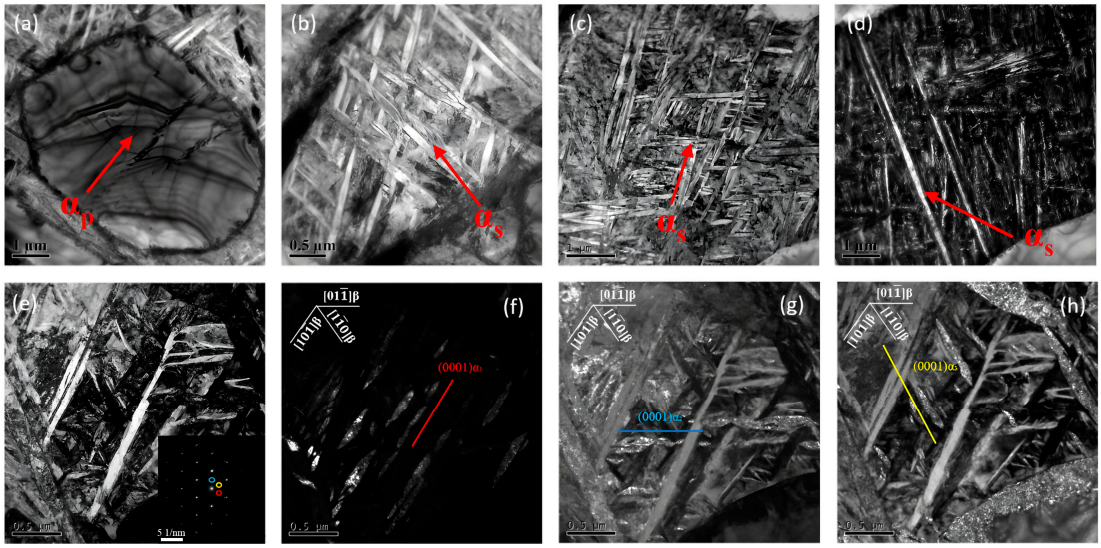


Figure 15. TEM analysis of the TC21 alloy after HIP at 980 °C/140 MPa for 3 h and subsequent heat treatment (900 °C/1 h/air cooling + 590 °C/4 h/air cooling): (**a**) BF image of coarse equiaxed α_p in the β matrix; (**b**–**d**) BF images of needle-like α_s in the β matrix; (**e**) DF image with the inset SAED pattern along the [111]β/[$2\bar{1}\bar{1}0$]α zone axes; (**f**–**h**) DF images of three α_s variants formed with g = (0001)α1, (0001)α2 and (0001)α3, respectively.

Figure 16 shows TEM images of the TC21 alloy HIPed at 1010 °C/140 MPa for 3 h, about 40 °C above the measured β transus of 970 ± 3 °C, followed by heat treatment at 900 °C/1 h/air cooling + 590 °C/4 h/air cooling. Lamellar α (α_L) with a long rod-like morphology is distributed alternately with the β matrix (Figure 16a). Owing to stress concentration in local regions, many straight dislocations and irregular deformation bands are present in the β matrix (Figure 16b). Slender needle-like α_s phases with a thickness of approximately 0.17 ± 0.04 μm are arranged in parallel within the field of view (Figure 16c). Figure 16d,e show that the lamellar α in this sample is characterized by fragmentation and dissolution: the lamellae, with an original thickness of about 0.4 ± 0.13 μm, break into smaller fragments, which is attributed to the re-dissolution of the α phase of the initial microstructure during HIP at 1010 °C; the SAED pattern taken from the fragment region (Figure 16f, zone axis [$1\bar{2}0$]α) confirms that the fragments retain the α structure. This is consistent with the EBSD observation in Figure 11, where the α within the coarse prior β grains originates from re-precipitation after partial dissolution

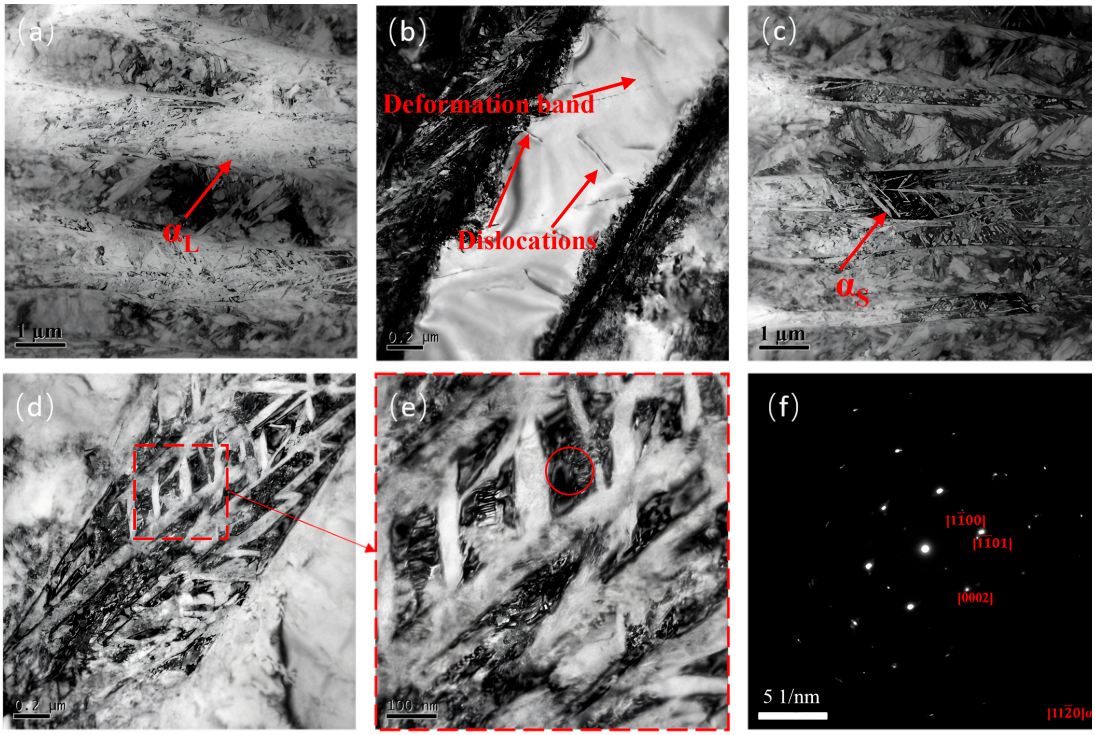


Figure 16. TEM analysis of the TC21 alloy after HIP at 1010 °C/140 MPa for 3 h (about 40 °C above the measured β transus of 970 ± 3 °C) and subsequent heat treatment (900 °C/1 h/air cooling + 590 °C/4 h/air cooling): (**a**) BF image of rod-like α_L alternating with the β matrix; (**b**) BF image showing dislocations and a deformation band in the β matrix; (**c**) BF image of parallel slender needle-like α_s; (**d**) BF image showing the fragmentation and dissolution of lamellar α; (**e**) enlarged view of the region marked by the red rectangle in (**d**); (**f**) SAED pattern taken from the region in (**e**), indexed along the [0001]α zone axis.

3.6. Mechanical Properties at Room Temperature

The tensile properties of the TC21 alloys in the as-HIPed state and after the identical solution and ageing treatment (900 °C/1 h/air cooling + 590 °C/4 h/air cooling) are summarized in Tables 2 and 3, respectively, and are compared in Figure 17c,d. The HIP temperature markedly affects the mechanical properties, but its influence differs between the two states.

In the as-HIPed state (Figure 17c, Table 2), both the yield strength and the ultimate tensile strength decrease monotonically with increasing HIP temperature, from 1032 to 908.5 ± 4.9 MPa and from 1133 ± 4.2 to 1039 ± 9.9 MPa, respectively (reductions of about 12% and 8%). This is consistent with the microstructural evolution revealed by SEM: a higher HIP temperature coarsens the α phase and increases the amount of retained β, thereby reducing the density of α/α and α/β interfaces that act as barriers to dislocation motion. In contrast, the ductility first increases and then decreases, reaching a maximum at 980 °C (elongation 18.25 ± 0.4%, reduction of area 52%) before dropping sharply at 1010 °C (9.75 ± 1.8% and 20%); the improvement up to 980 °C reflects the greater capacity of the coarser α and the larger β fraction to accommodate plastic strain, whereas at 1010 °C the alloy is fully transformed above the β transus and the resulting coarse basket-weave colonies provide little plastic accommodation.

After the solution and ageing treatment (Figure 17d, Table 3), the strength is substantially higher than in the as-HIPed state: the yield strength increases by 148–262 MPa and the ultimate tensile strength by 105–240 MPa, which is attributed to the precipitation of fine secondary α (α_s, 0.07–0.17 μm) within the β matrix during solution treatment, cooling

and ageing (Figures 12–16). Notably, the trend with HIP temperature is reversed: the ultimate tensile strength and yield strength increase from 1238.5 ± 2.1 and 1180 ± 1.4 MPa at 890 °C to 1278.5 ± 10.6 and 1211 ± 14.1 MPa at 980 °C, and then decrease to 1201 ± 9.5 and 1126 ± 9.9 MPa at 1010 °C. The increase from 950 to 980 °C, however, is marginal (1.5% in UTS and 1.3% in YS), while the ductility decreases markedly over the same interval, the elongation and reduction of area falling from 13 ± 2.82% and 35.5 ± 2.12% to 8.75 ± 1.76% and 29.5 ± 4.94% (reductions of 33% and 17%). With a further increase to 1010 °C, the elongation and reduction of area drop abruptly to 4 ± 1.41% and 9.5 ± 0.7%, and the strength also decreases. Consequently, the alloy HIPed at 950 °C combined with the solution and ageing treatment exhibits the best strength–ductility balance (UTS 1259.5 ± 3.63 MPa, YS 1195.5 ± 3.5 MPa, elongation 13 ± 2.82%, reduction of area 35.5 ± 2.12%). Its higher ductility relative to the 980 and 1010 °C conditions originates from the finer α phase and the absence of continuous grain-boundary α, which favour homogeneous plastic deformation, whereas the coarse α colonies and coarsened prior β grains formed at and above the β transus promote strain localisation and early void nucleation at the α/β interfaces.

Figure 17e compares the tensile properties obtained in this work with those reported for TC21 alloys processed by forging plus ageing [6,7], hot rolling and annealing [26], laser additive manufacturing [9], and other routes [27–30]. The 950 °C HIP condition combined with solution and ageing treatment lies in the upper-right region of the plot, outperforming most of the conventional wrought and additive-manufactured TC21 alloys in terms of the strength–ductility combination, which demonstrates that powder metallurgy HIP combined with solution and ageing treatment is an effective route for improving the mechanical properties of TC21.

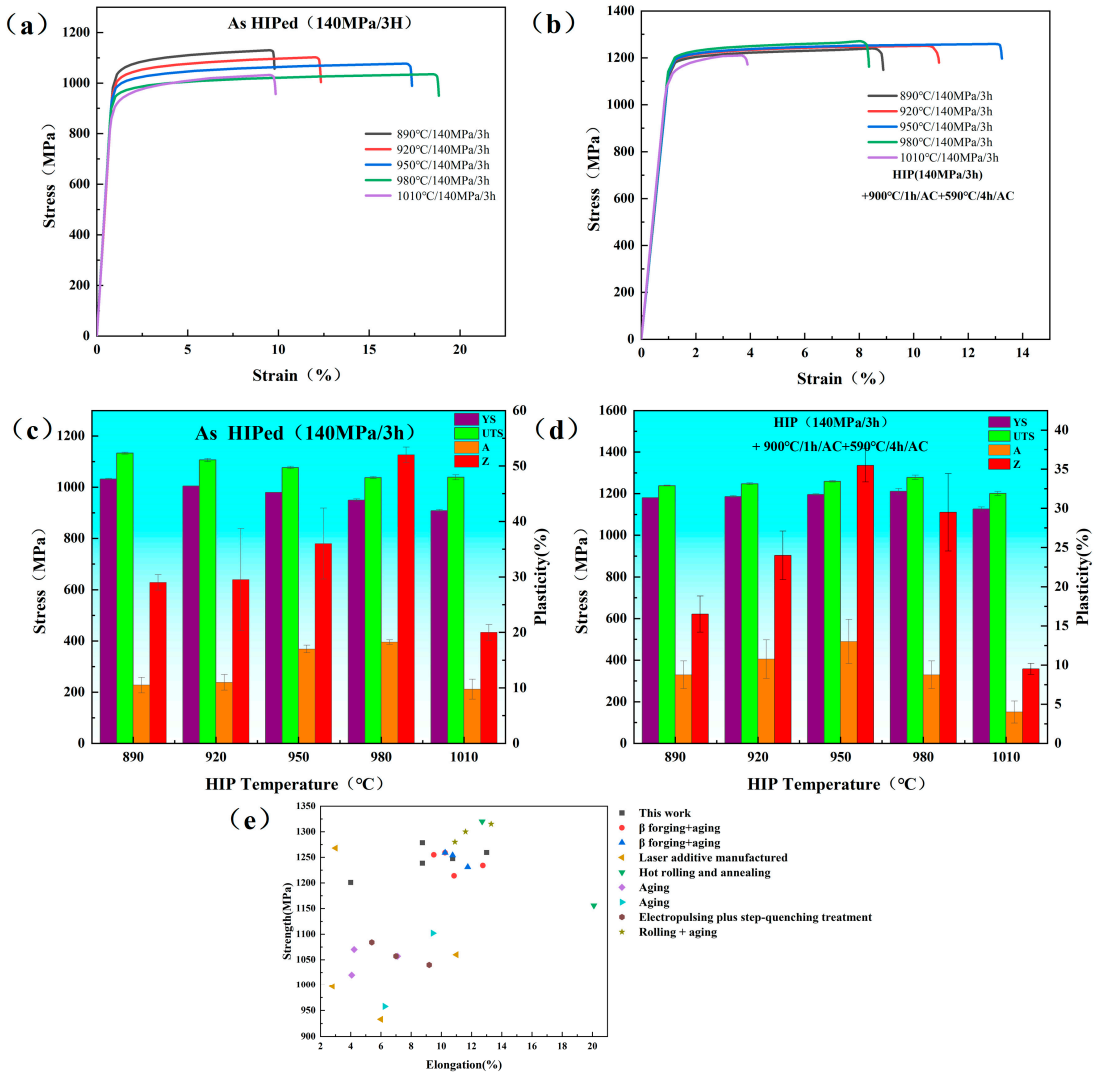


Figure 17. (**a**) Tensile stress–strain curves of the as-HIPed alloy (140 MPa/3 h). (**b**) Tensile stress–strain curves of the alloys HIPed at different temperatures (140 MPa/3 h) and subsequently heat-treated at 900 °C/1 h/air cooling + 590 °C/4 h/air cooling. (**c**) Mechanical Properties of As HIPed TC21. (**d**) Mechanical Properties of the TC21 alloys HIPed at different temperatures (140 MPa/3 h) and subsequently heat-treated at 900 °C/1 h/air cooling + 590 °C/4 h/air cooling. (**e**) Echanical properties after heat treatment: present work vs. reported TC21 alloys, adapted from [6,7,9,26–30].

The above results indicate that the microstructure has a significant influence on the mechanical properties. In the present alloy, however, the HIP temperature modifies the size of the equiaxed α (α_P) and the size and volume fraction of the secondary α (α_s) simultaneously, so that these two microstructural scales cannot be varied independently. The α size is therefore a proxy for the HIP temperature rather than an independent variable, The origin of these two opposite trends is discussed in Section 4.1.

The relative contributions of the individual mechanisms can nevertheless be assessed. Grain-boundary strengthening follows a Hall–Petch dependence on $d\alpha_P$, and the coarsening of α_P from 8.4 ± 1.31 μm (890 °C) to 15.7 ± 2.53 μm (980 °C) would, taken alone, lower the yield strength by about 30–45 MPa when the Hall–Petch slope reported for α-Ti and Ti–6Al–4V ($k_y \approx 0.3$–0.5 MPa·m$^{1/2}$) is used [31]. The measured strength, in contrast, increases over the same interval (YS: 1180 ± 1.4 → 1211 ± 14.1 MPa, UTS: 1238.5 ± 2.1 → 1278.5 ± 10.6 MPa), which demonstrates that the softening caused by coarsening is overcompensated by the strengthening associated with α_s. Between 890 and 950 °C a higher HIP temperature increases the amount of β retained after HIP (19–26%, Figures 7b–9b)

and hence the amount of α_s precipitated during the subsequent ageing treatment, so that the α_s/β interfacial area per unit volume increases and the effective slip length decreases. The α_s precipitates coarsen at the same time (mean thickness 0.07–0.10 μm over this interval, Table 3), so the net increase in the interfacial area is smaller than the increase in the precipitated amount alone would give; the interfacial term nevertheless dominates the response of the alloy up to 950 °C [32]. At 980 °C the retained β fraction falls back to 20% (Figure 10b) while the α_s coarsens further to 0.13 ± 0.06 μm, and the further rise in strength is then attributed to the fine, densely interlaced basket-weave lamellae (Figures 5g–h and 10a).

When the HIP temperature reaches 1010 °C, the alloy no longer follows this trend: the yield strength drops to 1126 ± 9.9 MPa and the elongation to 4%. The α_p coarsening from 15.7 ± 2.53 to 20.7 ± 2.12 μm accounts for only a small part of this loss (≈ 10–16 MPa); the remainder is attributed to the formation of a coarse Widmanstätten structure with continuous β films along the α boundaries and to the much lower density of α_s/β interfaces [32], which together restore a long effective slip length. The strength of the alloy therefore results from the competition between the softening caused by the coarsening of α_p and the interfacial strengthening provided by α_s, with the latter controlling the response in the range 890–950 °C.

3.7. Fracture Morphology

Figure 18 shows the fracture surfaces of the specimens after HIP at different temperatures and subsequent heat treatment (900 °C/1 h/air cooling + 590 °C/4 h/air cooling). All the specimens tested after HIP at 890–980 °C (Figure 18a–d) fail by microvoid coalescence: their fracture surfaces are covered by dimples of varying size together with tear ridges, indicating that the fracture mode remains ductile over this temperature range. The differences between the four conditions lie mainly in the size distribution of the dimples and in the development of the tear ridges. Among them, the specimen HIPed at 950 °C (Figure 18c) exhibits the coarsest and most uniformly distributed dimples and the thickest, most continuous tear ridges, indicating that the matrix accommodated a large amount of plastic deformation before final separation. This is consistent with the tensile results, in which this specimen shows the best ductility of the five conditions (A = 13 ± 2.82%, Z = 35.5 ± 2.12%, Table 3 and Figure 17d). With a further increase in the HIP temperature to 980 °C (Figure 18d), the dimples become shallower and less uniform and the number of secondary cracks increases, indicating that plastic deformation becomes more localized. When the HIP temperature reaches 1010 °C (Figure 18e), the fracture surface is dominated by river-patterned cleavage-like features, i.e., the fracture mode changes from ductile to quasi-cleavage. This change accounts for the sharp loss of ductility of this specimen (A = 4 ± 1.41%, Z = 9.5 ± 0.7%) and is attributed to the coarse Widmanstätten α colonies and to the continuous β films along the prior β boundaries, which provide long and weakly bonded paths for crack propagation.

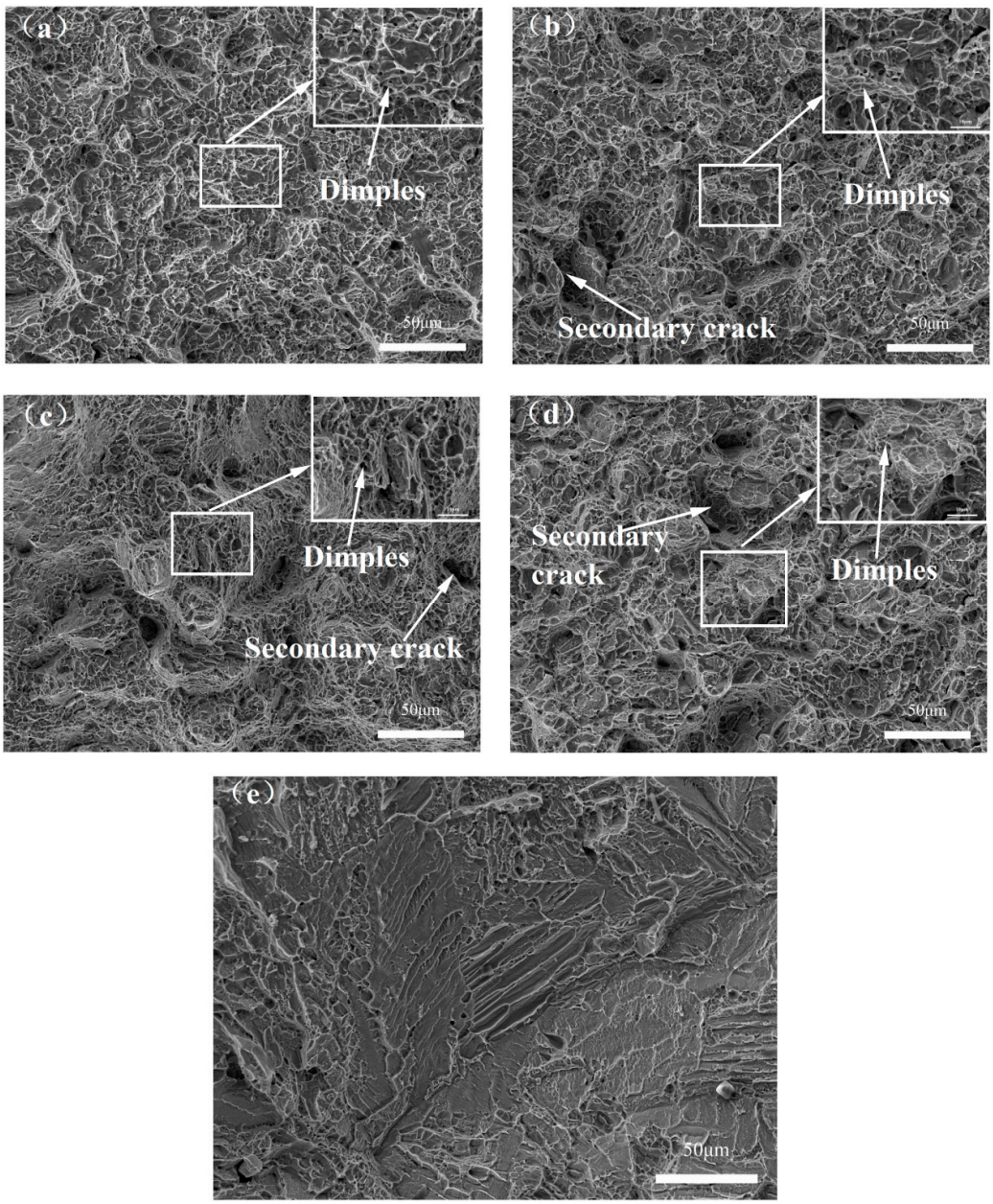


Figure 18. Fracture surfaces of the TC21 alloy after HIP at (**a**) 890 °C, (**b**) 920 °C, (**c**) 950 °C, (**d**) 980 °C and (**e**) 1010 °C and subsequent heat treatment (900 °C/1 h/air cooling + 590 °C/4 h/air cooling); (**a**–**d**) show dimpled fracture with tear ridges (microvoid coalescence); (**e**) shows river-patterned cleavage-like features.

4. Discussion

4.1. Effect of HIP Temperature on the Strength of the Alloy

The α/β interfaces hinder dislocation motion and therefore contribute to the strength of the alloy [20,32]. After the heat treatment (900 °C/1 h/AC + 590 °C/4 h/AC), the yield strength and the ultimate tensile strength increase from 1180 ± 1.4 and 1238.5 ± 2.1 MPa at 890 °C to 1195.5 ± 3.5 and 1259.5 ± 3.63 MPa at 950 °C, remain essentially unchanged up to 980 °C (1211 ± 14.1 and 1278.5 ± 10.6 MPa), and then decrease to 1126 ± 9.9 and 1201 ± 9.5 MPa at 1010 °C (Table 3). The strength of the as-HIPed alloy, in contrast, decreases monotonically as the HIP temperature rises (YS 1032 ± 2.8 → 908.5 ± 4.9 MPa, Table 2). The two opposite trends show that the strength of the heat-treated alloy is not controlled by the as-HIPed microstructure itself, but by the α_s precipitated during the subsequent

ageing treatment—by how much α_s forms and how it is distributed in the β matrix—which in turn depends on how much α_p has been dissolved during HIP.

Between 890 and 950 °C, raising the HIP temperature promotes the dissolution of αp into the β matrix, and the β fraction increases from 19% at 890 °C to 26% at 950 °C (Figures 7b–11b). The α-stabilising elements released by the dissolving α_p increase the supersaturation of the β matrix and hence the driving force for the precipitation of α_s during ageing, so that a larger amount of α_s is precipitated and the α_s/β interfacial area per unit volume increases, even though the α_s coarsens slightly (0.07 ± 0.01 → 0.10 ± 0.05 μm, Table 3). From 950 to 980 °C the strength remains essentially unchanged, consistent with the opposing trends of the β fraction (26% → 20%, Figures 9b and 10b) and of the α_s thickness (0.10 ± 0.05 → 0.13 ± 0.06 μm, Table 3) over this interval. It should be noted that the HIP temperature modifies the size of α_p and the size and volume fraction of α_s simultaneously, so that the α size is a proxy for the HIP temperature rather than an independent variable; a Hall–Petch type analysis based on the α size alone is therefore not applicable to the present data set and is not reported here.

For α/β lamellar interfaces the Hall–Petch coefficient has been theoretically estimated to be ≈ 272.6 MPa·μm$^{1/2}$ [32]. This is of the same order as, though somewhat lower than, the grain-boundary coefficient (0.3–0.5 MPa·m$^{1/2}$ [31]); the decisive difference is the length scale that enters the relation, namely, the αs thickness (0.07 ± 0.01–0.17 ± 0.04 μm, Table 3) instead of the α_p size (8.4 ± 1.31–20.7 ± 2.12 μm), which makes the corresponding d$^{-1/2}$ term about one order of magnitude larger. The relation should not, however, be applied quantitatively to the present data set, because the α size is not an independent variable (Section 3.6); it is used here only to show that the α_s/β interfaces, rather than the α_p boundaries, control the strength in the range 890–950 °C.

When the HIP temperature reaches 1010 °C, about 40 °C above the β transus (970 ± 3 °C), α dissolves completely into the β matrix and the β grains coarsen considerably. During the subsequent heat treatment, grain-boundary α precipitates first along the prior β boundaries and lamellar α colonies then grow inward, replacing the fine α_s. The α_s/β interfacial area per unit volume decreases sharply and the effective slip length increases again, while the continuous β films retained along the α boundaries provide long and weakly bonded paths for localized deformation. The coarsening of α from 15.7 ± 2.53 to 20.7 ± 2.12 μm accounts for only ≈ 10–16 MPa of the loss [31], and the strength therefore drops to 1126 ± 9.9 MPa (YS) and 1201 ± 9.5 MPa (UTS). The strength of the alloy is thus the result of a competition between the softening caused by the coarsening of α and the interfacial strengthening provided by αs, with the latter controlling the response between 890 and 980 °C.

4.2. Effect of HIP Temperature on the Ductility of the Alloy

After the heat treatment, the ductility reaches its maximum at a HIP temperature of 950 °C (A = 13 ± 2.82%, Z = 35.5 ± 2.12%) and collapses at 1010 °C (A = 4 ± 1.41%, Z = 9.5 ± 0.7%) (Table 3).

The effect of the HIP temperature on the ductility cannot be fully understood without considering the area of the α/β interfaces, which is the microstructural parameter shared by the strengthening and the deformation behaviour. The interfacial area per unit volume can be estimated from stereological relations, Sv ≈ 6f/d for equiaxed particles and Sv ≈ 2f/t for lamellae, where f is the volume fraction and d (or t) the characteristic size of the corresponding phase [33]. The interfacial area is thus governed by the volume fraction and the characteristic size at the same time, and these two quantities do not vary in the same direction with the HIP temperature. Between 890 and 950 °C, the progressive dissolution of α_p increases the β fraction from 19% to 26% (Figures 7b–11b), and the subsequent ageing precipitates an increasing amount of fine α_s; both the volume fraction and the number

density of α_s increase while its thickness remains sub-micrometre (0.07–0.10 ± 0.05 μm, Table 3), so that the α_s/β interfacial area increases markedly. This tendency is not maintained at 980 °C, where the retained β fraction decreases to 20% (Figure 10b) and the α_s coarsens to 0.13 ± 0.06 μm (Table 3), so that the α_s/β interfacial area no longer increases.

The interfacial area influences the ductility in two opposite ways. On the one hand, each α_s/β and α_p/β interface acts as an obstacle to dislocation motion, and the multiplicity of interfaces with different orientations forces dislocations to change their slip systems repeatedly, which distributes the plastic strain over the whole volume and delays strain localization; the interfaces also provide sites for the accumulation of dislocations and thus sustain work hardening during uniform deformation. As shown in Figure 19a, the equiaxed α_p possesses a good ability to deform plastically, and its rotation accommodates the deformation and provides space for dislocation slip [34]. On the other hand, a high density of interfaces also concentrates stress: dislocations pile up at the α_p/β interfaces, the local stress is raised and microcracks are nucleated there [14]. The ductility therefore does not increase monotonically with the interfacial area; an optimum is expected when the interfaces are fine, numerous and uniformly distributed, which is the case for the specimen HIPed at 950 °C. Although the α_s coarsens slightly as the HIP temperature rises, the simultaneous increase in its amount keeps the interfacial area high and thus offsets the adverse effect of the coarsening.

Above 950 °C the ductility decreases continuously. When the HIP temperature reaches 1010 °C, the microstructure is dominated by a Widmanstätten structure consisting of coarse prior β grains, continuous grain-boundary α and lamellar α colonies (Figure 19b). The continuous grain-boundary α weakens the bonding of the boundaries, and the lamellar α colonies restrict dislocation slip and deformation coordination [35,36]. Dislocations pile up at the colony and grain boundaries, and the resulting high back stress initiates cracks there and drives their propagation; because the continuous grain-boundary α provides a long and weakly bonded path, the crack propagates without deflection and the specimen fails prematurely. In agreement with this, the fracture surface changes from dimpled (microvoid coalescence) at 890–980 °C to river-patterned cleavage-like features at 1010 °C (Figure 18). The alloy therefore exhibits a poor capability of uniform deformation and a low resistance to necking, and both the elongation and the reduction of area decrease, to 4 ± 1.41% and 9.5 ± 0.7% respectively.

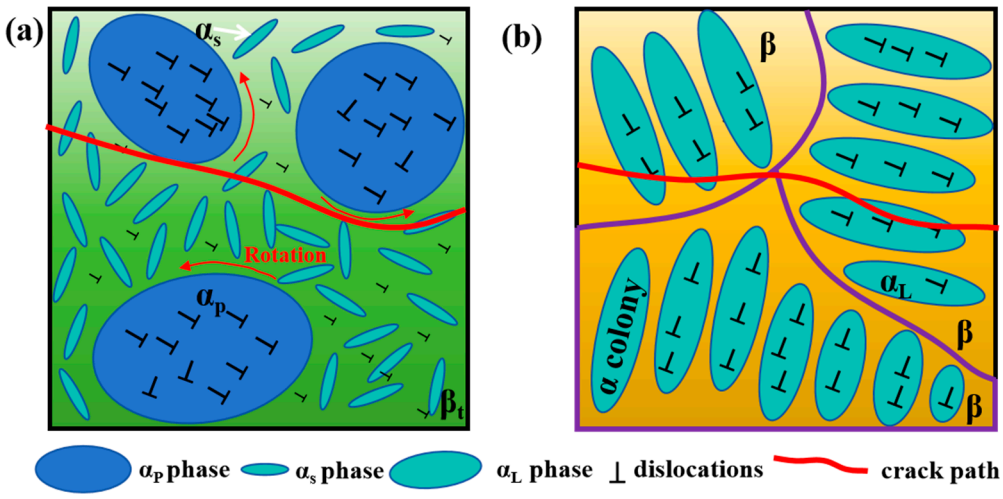


Figure 19. Schematic diagrams of the deformation and fracture mechanisms at different HIP temperatures (140 MPa/3 h) after heat treatment (900 °C/1 h/air cooling + 590 °C/4 h/air cooling): (**a**) 890–980 °C; (**b**) 1010 °C.

5. Conclusions

1. After HIP and the subsequent solution and ageing treatment, the TC21 alloy consists of α_p, α_s and retained β. Below the β transus (970 ± 3 °C), raising the HIP temperature from 890 to 950 °C promotes the dissolution of α_p, increases the β fraction from 19% to 26% and leads to the precipitation of a larger amount of α_s during ageing, although the α_s also coarsens (0.07 ± 0.01 → 0.13 ± 0.06 μm). Above the transus (980 and 1010 °C), a coarse Widmanstätten structure with continuous grain-boundary α forms.
2. In the as-HIPed state the strength decreases monotonically with increasing HIP temperature (YS: 1032 ± 2.8→908.5 ± 4.9 MPa), whereas after the heat treatment it increases from 890 to 980 °C(YS: 1180 ± 1.4→1211 ± 14.1 MPa) and drops sharply at 1010 °C (1126 ± 9.9 MPa). The strengthening is dominated by the interfacial strengthening of the fine α_s, which outweighs the softening caused by the coarsening of α_p.
3. The ductility is governed by the α/β interfacial area, which acts in two opposite ways: it distributes the plastic strain and sustains work hardening, but also concentrates stress and nucleates microcracks. The ductility therefore peaks at 950 °C (A = 13 ± 2.82%, Z = 35.5 ± 2.12%), where the interfaces are fine and uniformly distributed, and collapses at 1010 °C (A = 4 ± 1.41%, Z = 9.5 ± 0.17%) as the interfacial area decreases and the fracture mode changes to quasi-cleavage.
4. The optimum combination of strength and ductility is obtained at a HIP temperature of 950 °C: UTS 1259.5 ± 3.63 MPa, YS 1195.5 ± 3.5 MPa, A 13 ± 2.82% and Z 35.5 ± 2.12%. Although the highest strength is reached at 980 °C, the elongation falls to 8.75% there; HIP at 950 °C is therefore recommended.

Author Contributions: Conceptualization, H.Z., J.Y., Z.Q. and H.W.; methodology, H.Z. and C.L.; validation, C.L. and Z.Q.; formal analysis, C.L., Z.Q. and W.L.; investigation, C.L., Z.Q. and H.W.; resources, J.Y.; data curation, Z.Q., K.H. and H.W.; writing—original draft, H.Z.; writing—review & editing, C.L., J.Y., Z.Q., K.H., H.W. and W.L.; visualization, Z.Q., K.H. and W.L.; supervision, J.Y., Z.Q. and K.H. All authors have read and agreed to the published version of the manuscript.

Funding: This research received no external funding.

Data Availability Statement: The original contributions presented in this study are included in the article. Further inquiries can be directed to the corresponding author.

Conflicts of Interest: Chenyang Li, Jun Yin and Zhuan Qi were employed by the Yinchuang Aerospace Industry (Jiangsu) Co., Ltd., Wu'xi 214000, China. The remaining authors declare that the research was conducted in the absence of any commercial or financial relationships that could be construed as a potential conflict of interest.

References

1. Wang, K.; Li, M. Characterization of discontinuous yielding phenomenon in isothermal compression of TC8 titanium alloy. *Trans. Nonferrous Met. Soc. China* **2016**, *26*, 1583–1588. https://doi.org/10.1016/S1003-6326(16)64234-6.
2. Fan, X.; Zeng, X.; Yang, H.; Gao, P.; Meng, M.; Zuo, R.; Lei, P. Deformation banding in β working of two-phase TA15 titanium alloy. *Trans. Nonferrous Met. Soc. China* **2017**, *27*, 2390–2399. https://doi.org/10.1016/S1003-6326(17)60265-6.
3. Banerjee, D.; Williams, J.C. Perspectives on Titanium Science and Technology. *Acta Mater*. **2013**, *61*, 844–879. https://doi.org/10.1016/j.actamat.2012.10.043.
4. Zhao, Y.; Qu, H. Research on High Strength and High Toughness Titanium Alloy with Damage Tolerance. *Titanium Ind. Prog*. **2010**, *654–656*, 586–589. https://doi.org/10.4028/www.scientific.net/MSF.654-656.586.
5. Qu, H.; Zhou, Y.; Zhou, L.; Zhao, Y.; Zeng, W.; Feng, L. Relationship among forging technology, structure and properties of TC21 alloy bars. *Trans. Nonferrous Met. Soc. China* **2005**, *15*, 1120–1124.

6. Li, X.; Huang, C.; Yang, J.; Liu, F.; Wei, S.; Wan, M.; Zhao, F.; Zhao, Y. Optimization of quasi-β forging parameters to control trimodal microstructure parameters and performance of TC21 forgings. *Mater. Sci. Eng. A* **2024**, *909*, 146824. https://doi.org/10.1016/j.msea.2024.146824.
7. Li, X.; Huang, C.; Ye, X.; Yang, J.; Wan, M.; Liu, D. Effect of aging temperatures on the microstructure and mechanical properties of TC21 forgings with basket–weave microstructure. *Mater. Charact.* **2024**, *216*, 114270. https://doi.org/10.1016/j.matchar.2024.114270.
8. Zhu, Y.C.; Zeng, W.D.; Liu, J.L.; Zhao, Y.Q.; Zhou, Y.G.; Yu, H.Q. Effect of processing parameters on the hot deformation behavior of as-cast TC21 titanium alloy. *Mater. Des.* **2012**, *33*, 264–272. https://doi.org/10.1016/j.matdes.2011.07.018.
9. Zhang, Q.; Chen, J.; Zhao, Z.; Tan, H.; Lin, X.; Huang, W. Microstructure and anisotropic tensile behavior of laser additive manufactured TC21 titanium alloy. *Mater. Sci. Eng. A* **2016**, *673*, 204–212. https://doi.org/10.1016/j.msea.2016.07.040.
10. Chen, G.; Wang, Z.; Li, Z.; Chang, X.; Chen, Q.; Xia, C.; Wang, Y.; Qi, Y. Mechanical properties and isotropy of quasi-β forged Ti-6Al-2Sn-3Mo-1Cr-2Zr-2Nb alloy dominated by boundary development and dynamic lath precipitation. *Mater. Sci. Eng. A* **2026**, *960*, 150115. https://doi.org/10.1016/j.msea.2026.150115.
11. Singh, G.; Sen, I.; Gopinath, K.; Ramamurty, U. Influence of minor addition of boron on tensile and fatigue properties of wrought Ti-6Al-4V alloy. *Mater. Sci. Eng.* **2012**, *540*, 142–151. https://doi.org/10.1016/j.msea.2012.01.119.
12. Yan, M.; Yang, F.; Lu, B.; Chen, C.; Sui, Y.; Guo, Z. Microstructure and Mechanical Properties of High Relative Density γ-TiAl Alloy Using Irregular Pre-Alloyed Powder. *Metals* **2021**, *11*, 635. https://doi.org/10.3390/met11040635.
13. Song, M.; Zhang, Y.; Yang, Y.; Li, Y.; Yang, H.; Wang, Y.; Zhang, X. Spherical TiAl alloy powders by prep: Preparation, microstructure and properties. *J. Phys. Conf. Ser.* **2023**, *2639*, 012011. https://doi.org/10.1088/1742-6596/2639/1/012011.
14. Cai, C.; Song, B.; Xue, P.; Wei, Q.; Yan, C.; Shi, Y. A novel near alpha-Ti alloy prepared by hot isostatic pressing: Microstructure evolution mechanism and high temperature tensile properties. *Mater. Des.* **2016**, *106*, 371–379. https://doi.org/10.1016/j.matdes.2016.05.092.
15. Xu, L.; Guo, R.; Bai, C.; Lei, J.; Yang, R. Effect of Hot Isostatic Pressing Conditions and Cooling Rate on Microstructure and Properties of Ti–6Al–4V Alloy from Atomized Powder. *J. Mater. Sci. Technol.* **2014**, *30*, 1289–1295. https://doi.org/10.1016/j.jmst.2014.04.011.
16. Fang, Z.Z.; Paramore, J.D.; Sun, P.; Chandran, K.S.R.; Zhang, Y.; Xia, Y.; Cao, F.; Koopman, M.; Free, M. Powder metallurgy of titanium-past, present, and future. *Int. Mater. Rev.* **2018**, *63*, 407–459. https://doi.org/10.1080/09506608.2017.1366003.
17. Zhang, K.; Mei, J.; Wain, N.; Wu, X. Effect of hot-isostatic-pressing parameters on the microstructure and properties of powder Ti–6Al–4V hot-isostatically-pressed samples. *Metall. Mater. Trans. A* **2010**, *41*, 1033–1045. https://doi.org/10.1007/s11661-009-0149-y.
18. Zhu, L.; Pan, Y.; Liu, Y.; Sun, Z.; Wang, X.; Nan, H.; Mughal, M.-A.; Lu, D.; Lu, X. Effects of microstructure characteristics on the tensile properties and fracture toughness of TA15 alloy fabricated by hot isostatic pressing. *Int. J. Miner. Metall. Mater.* **2023**, *30*, 697–706. https://doi.org/10.1007/s12613-021-2371-6.
19. Zhang, X.; Jia, W.; Mao, X. Effect of microstructure on the tensile properties and impact toughness of TC21G titanium alloy. *Mater. Charact.* **2022**, *185*, 111752. https://doi.org/10.1016/j.matchar.2022.111752.
20. Zhu, W.; Tan, C.; Xiao, R.; Sun, Q.; Sun, J. Slip behavior of Bi-modal structure in a metastable β titanium alloy during tensile deformation. *J. Mater. Sci. Technol.* **2020**, *57*, 188–196. https://doi.org/10.1016/j.jmst.2020.03.053.
21. Huang, C.; Zhao, Y.; Xin, S.; Zhou, W.; Li, Q. Effect of microstructure on tensile properties of Ti-5Al-5Mo-5V-3Cr-1Zr alloy. *J. Alloys Compd.* **2017**, *693*, 582–591. https://doi.org/10.1016/j.jallcom.2016.09.233.
22. Wang, Y.; Xue, X.; Kou, H.; Chang, J.; Yin, Z.; Li, J. Improvement of microstructure homogenous and tensile properties of powder hot isostatic pressed TA15 titanium alloy via heat treatment. *Mater. Lett.* **2022**, *311*, 131585. https://doi.org/10.1016/j.matlet.2021.131585.
23. Gao, P.; Cai, Y.; Zhan, M.; Fan, X.; Lei, Z. Crystallographic orientation evolution during the development of tri-modal microstructure in the hot working of TA15 titanium alloy. *J. Alloys Compd.* **2018**, *741*, 734–745. https://doi.org/10.1016/j.jallcom.2018.01.222.
24. Stanford, N.; Bate, P.S. Crystallographic variant selection in Ti–6Al–4V. *Acta Mater.* **2004**, *52*, 5215–5224. https://doi.org/10.1016/j.actamat.2004.07.034.
25. GB/T 228.1-2021; Metallic materials—Tensile testing—Part 1: Method of test at room temperature. Standards Press of China: Beijing, China, 2021
26. Li, H.; Wang, K.; Xin, L.; Xin, R.; Liu, Q. Effect of hot rolling and annealing on phase component, recrystallization, and mechanical properties of TC21 titanium alloy. *J. Mater. Eng. Perform.* **2022**, *31*, 2496–2508. https://doi.org/10.1007/s11665-021-06351-6.

27. Ye, X.; Wan, M.; Huang, C.; Lei, M.; Jian, S.; Zhang, Y.; Xu, D.; Huang, F. Effect of aging temperature on mechanical properties of TC21 alloy with multi-level lamellar microstructure. *Mater. Sci. Eng. A* **2022**, *840*, 142825. https://doi.org/10.1016/j.msea.2022.142825.
28. Fan, Y.; Tan, C.; Huang, C.; He, J.; Pan, Y.; Wen, L.; Lu, H.; Zhang, G. Strength and ductility improvement of the axial gradient microstructure TC21 titanium alloys manufactured by electropulsing plus step-quenching treatment. *J. Alloys Compd.* **2024**, *984*, 173979. https://doi.org/10.1016/j.jallcom.2024.173979.
29. Wang, J.; Ye, X.; Li, Y.; Wan, P.; Huang, C.; Huang, F.; Lei, M.; Liu, D.; Ma, R.; Ren, X. Effect of annealing temperature on mechanical properties of TC21 titanium alloy with multilevel lamellar microstructure. *Mater. Sci. Eng. A* **2023**, *869*, 144788. https://doi.org/10.1016/j.msea.2023.144788.
30. Wang, S.; Liang, Y.; Sun, H.; Feng, X.; Huang, C. Thermomechanical treatment-induced microstructure refinement to optimize mechanical properties of TC21 titanium alloys. *Mater. Sci. Eng. A* **2021**, *812*, 141095. https://doi.org/10.1016/j.msea.2021.141095.
31. Takebe, H.; Ushioda, K. Effects of Grain Size, Thickness and Tensile Direction on Yield Behavior of Pure Titanium Sheet. *Mater. Trans*. **2023**, *64*, 86–94. https://doi.org/10.2320/matertrans.MT-MLA2022002.
32. Wang, F.; Luo, X.M.; Lei, L.M.; Fu, X.; Zhang, B.; Zhang, G.p. Theoretical Evaluation of Strengthening Ability of Phase Interfaces in Lamellar Ti Alloys. *Adv. Eng. Mater*. **2021**, *24*, 2101570. https://doi.org/10.1002/adem.202101570.
33. Underwood, E.E. Quantitative Stereology for Microstructural Analysis. In *Microstructural Analysis: Tools and Techniques*; Springer: Boston, MA, USA, 1973. https://doi.org/10.1007/978-1-4615-8693-7_3.
34. Wei, L.; Mei, G.; Xi, M.; Yi, L. In situ deformation behavior of TC21 titanium alloy with different alpha morphologies (equi-axed/lamellar). *Rare Met*. **2021**, *40*, 1173–1181. https://doi.org/10.1007/s12598-020-01657-1.
35. Wen, X.; Wan, M.; Huang, C.; Lei, M. Strength and fracture toughness of TC21 alloy with multi-level lamellar microstructure. *Mater. Sci. Eng. A* **2019**, *740–741*, 121–129. https://doi.org/10.1016/j.msea.2018.10.056.
36. Bai, J.K.; Zhang, H.; Zhao, Z.B.; Yang, R.D.; Zhang, S.Z.; Chen, T.; Zhang, X.Y.; Liang, S.X.; Liu, R.P. Strong and plastic near-α titanium alloy by Widmansttten structure spheroidization. *J Mater Sci Technol*. **2025**, *225*, 95–110. https://doi.org/10.1016/j.jmst.2024.12.018.

Disclaimer/Publisher's Note: The statements, opinions and data contained in all publications are solely those of the individual author(s) and contributor(s) and not of MDPI and/or the editor(s). MDPI and/or the editor(s) disclaim responsibility for any injury to people or property resulting from any ideas, methods, instructions or products referred to in the content.